

# Radiation from relativistic jets in blazars and the efficient dissipation of their bulk energy via photon breeding

Boris E. Stern<sup>1,2,3\*</sup> and Juri Poutanen<sup>3\*</sup>

<sup>1</sup>*Institute for Nuclear Research, Russian Academy of Sciences, Prospekt 60-letiya Oktyabrya 7a, Moscow 117312, Russia*

<sup>2</sup>*Astro Space Center, Lebedev Physical Institute, Profsoyuznaya 84/32, Moscow 117997, Russia*

<sup>3</sup>*Astronomy Division, Department of Physical Sciences, P.O.Box 3000, FIN-90014 University of Oulu, Finland*

Accepted, Received

## ABSTRACT

High-energy photons propagating in the magnetised medium with large velocity gradients can mediate energy and momentum exchange. Conversion of these photons into electron-positron pairs in the field of soft photons with the consequent isotropization and emission of new high-energy photons by Compton scattering can lead to the runaway cascade of the high-energy photons and electron-positron pairs fed by the bulk energy of the flow. This is the essence of the photon breeding mechanism.

We study the problem of high-energy emission of relativistic jets in blazars via photon breeding mechanism using 2D ballistic model for the jet with the detailed treatment of particle propagation and interactions. Our numerical simulations from first principles demonstrate that a jet propagating in the soft radiation field of broad emission line region can convert a significant fraction (up to 80 per cent) of its total power into radiation.

We show that the gamma-ray background of similar energy density as observed at Earth is sufficient to trigger the photon breeding. The considered mechanism produces a population of high-energy electrons (and positrons) and, therefore, alleviates the need for alternative (Fermi-type) particle acceleration models that have not yet been shown to produce high-energy leptons self-consistently. The mechanism reproduces basic spectral features observed in blazars including the blazar sequence (shift of spectral peaks towards lower energies with increasing luminosity). The significant deceleration of the jet at subparsec scales and the transversal gradient of the Lorentz factor (so called structured jet) predicted by the model reconcile the discrepancy between the high Doppler factors determined by the fits to the spectra of TeV blazars and the low apparent velocities observed at VLBI scales. The mechanism produces significantly broader angular distribution of radiation than that predicted by a simple model assuming the isotropic emission in the jet frame. This helps to reconcile the observed statistics and luminosity ratio of FR I and BL Lac objects with the large Lorentz factors of the jets as well as to explain the high level of the TeV emission in the radio galaxy M87.

We also discuss other possible sites of operation of the photon breeding mechanism and demonstrate that the accretion disc radiation at the scale of about 100 Schwarzschild radii and the infrared radiation from the dust at a parsec scale can serve as targets for photon breeding.

**Key words:** acceleration of particles – galaxies: active – BL Lacertae objects: general – galaxies: jets – gamma-rays: theory – radiation mechanisms: nonthermal

## 1 INTRODUCTION

The large gamma-ray isotropic luminosities of the powerful blazars  $10^{47}$ – $10^{49}$  erg s<sup>-1</sup> (Mukherjee et al. 1997) require a very powerful energy source. There is a general consensus that this emission is produced by relativistic jets emanating from the vicinity of a black hole. The beaming of radiation into a solid angle  $\Omega \sim 0.01$  str reduces the total luminosity to  $10^{45}$ – $10^{46}$  erg s<sup>-1</sup>, which is still

comparable to the bolometric luminosity of a luminous quasar. This implies a high efficiency of the bulk energy conversion into gamma-ray emission, because the accretion luminosity is similar to the jet power (Rawlings & Saunders 1991).

What kind of energy is available for high-energy radiation of blazars: the jet internal energy or the total energy carried by the jet through the external environment? The first scenario can be associated with the internal shocks (e.g. Rees 1978; Spada et al. 2001) or magnetic reconnection (see e.g. Lyutikov 2003). Then the efficiency is limited by the dispersion of the jet Lorentz factor or by

\* E-mail: stern@bes.asc.rssi.ru (BES), juri.poutanen@oulu.fi (JP)

the share of magnetic field which can reconnect, which depends on the field structure.

The second scenario provides a larger potential energy budget, but requires a “friction” between the jet and the external environment. A promising mechanism for such a friction can be associated with the exchange of neutral particles between the two media which move with respect to each other. The simplest version of such scenario is the exchange of photons by Compton scattering (Arav & Begelman 1992). If the energy flux in the quasar jet is dominated by cold protons then the Thomson optical depth across the jet (assuming one electron per proton) is

$$\tau_p(R) = \frac{L_j}{R_j} \frac{\sigma_T}{2\pi m_p c^3 \Gamma_j} \approx 2.3 \cdot 10^{-5} \frac{L_{j,45}}{R_{17} \theta \Gamma_j}, \quad (1)$$

where  $L_j$  is the jet power,  $R_j$  is the radius of the jet cross-section,  $R$  is the distance from the black hole,  $\theta = R_j/R$  and  $\Gamma_j$  are the jet opening angle and the initial Lorentz factor.<sup>1</sup> Such a small optical depth is insufficient to provide a considerable photon viscosity. However, the optical depth for high-energy photons against pair production on the low-energy photons can be high enough. For example, a luminous accretion disc of a quasar emitting soft radiation with luminosity  $L_d \sim 10^{45} \text{ erg s}^{-1}$  at a typical temperature  $\Theta = kT/m_e c^2 = 10^{-5}$ , provides a high opacity across the jet (see Stern & Poutanen 2006, hereafter SP06):

$$\tau_{\gamma\gamma}(R) = 60 \frac{L_{d,45}}{R_{17} \Theta^{-5}} (10\theta), \quad (2)$$

which remains more than unity up to the parsec scale.

Derishev et al. (2003) and Stern (2003) suggested a mechanism of dissipation of the bulk energy of relativistic fluids through the particle exchange with charge conversion (the converter mechanism). When this mechanism supplies energy to  $e^\pm$  pairs and photons, it can work in a runaway manner similar to a chain reaction in a supercritical nuclear pile. Here the role of breeding neutrons belongs to the high-energy photons, which extract energy from the fluid and breed exponentially. In this way the converter mechanism takes the form of a supercritical photon breeding (hereafter, photon breeding). Stern (2003) studied numerically the operation of the photon breeding mechanism in ultrarelativistic shocks propagating in a moderately dense environment, showing the high efficiency of the bulk energy dissipation. A similar problem for relativistic jets in active galactic nuclei (AGNs) was investigated by us (SP06), using a simple 1D ballistic model of the jet and a detailed treatment of particle propagation and interactions. We showed that up to 20 per cent of the jet kinetic energy can be converted into gamma-rays, if the following conditions are met: Lorentz factor above  $\sim 4$ , a sharp transition layer between the jet and the external environment, the presence of the ambient soft photon field, and a transversal or a chaotic, not very strong, magnetic field.

The present paper is a development of the approach presented in SP06. The main improvement is 2D treatment of the fluid (instead of 1D in SP06) and a better numerical resolution. The 2D treatment allows us to track the evolution of the system for much longer time, when it reaches a steady state. We also study the jet emission at a wider range of distances and with different sources of the soft photon background. We still neglect the internal pressure and treat the jet dynamics in a ballistic approximation.

In Section 2 we describe our model of the jet, the external soft radiation and the scheme of the numerical simulation. In Section

3 we describe the parameters of our simulations and present the results: the light curves of escaping photons, their spectra, distributions of the Lorentz factor of the decelerating jet, and the energy distribution of pairs produced in the jet. The properties of the model and its limitations are discussed in Sect. 4. In Section 5 we discuss the astrophysical implications of our model. We conclude in Section 6.

## 2 PROBLEM SETUP

### 2.1 Photon breeding mechanism

Let us first summarise the basic physics of the photon breeding mechanism in the context of relativistic jets (see SP06 for more details). Consider a jet with bulk Lorentz factor  $\Gamma_j$  propagating through the stationary medium. Assume that the medium is filled with the background soft photons (e.g. from the accretion disc, broad-emission line region, dusty torus, etc.) and some seed high-energy photons (e.g. extragalactic gamma-ray background). An external high-energy photon of energy  $\epsilon$  enters the jet and interacts with a soft (disc) photon producing an electron-positron pair.<sup>2</sup> The typical energy of the high-energy photon interacting with the blackbody radiation field of temperature  $\Theta$  is a few times  $\Theta^{-1}$ . The time-averaged Lorentz factor of the produced pair (as measured in the external frame) gyrating in the magnetic field of the jet, becomes  $\gamma \sim \Gamma_j^2 \epsilon \sim \Gamma_j^2 \Theta^{-1}$ . The electrons and positrons in the jet Comptonize soft photons (internal synchrotron or external) up to high energies.<sup>3</sup> Some of these photons leave the jet and produce pairs in the external environment, which gyrate in the magnetic field and Comptonize soft photons more or less isotropically. Some of these Comptonized high-energy photons enter the jet again.

In this cycle, the energy gain,  $\sim \Gamma_j^2$ , is provided by the isotropization of the charged particles in the jet frame and is taken from the bulk energy of the flow. Other steps in the cycle are energy sinks. The whole process proceeds in a runaway regime, with the total energy in photons and relativistic particles increasing exponentially, if the amplification coefficient (energy gain in one cycle) is larger than unity. As shown in SP06, the amplification coefficient is  $A \lesssim \Gamma_j^2/10$ , implying the minimum Lorentz factor of the flow needed for the process to operate  $\Gamma_j \sim 4$ . This theoretical minimum is, however, difficult to reach as other conditions should be met.

The preferred conditions are: the weak jet magnetic field (which reduces the energy sink by synchrotron radiation) and large energy density of the external isotropic radiation in the jet frame (which increases the Compton losses). The latter requirement translates into high  $\Gamma_j$  and/or high fraction of the disc radiation scattered/reprocessed in the ambient medium. A sufficiently sharp boundary between the jet and the external environment also increases the efficiency of the process, however, as we show in this paper, it is not a necessary condition.

<sup>2</sup> The photon energies, in units of the electron rest mass  $m_e c^2$ , are denoted as  $x$  and  $\epsilon$  for photons of low ( $< 1$ ) and high ( $> 1$ ) energies, respectively. We define also the power-law index  $\alpha \equiv -d \log F(x)/d \log x$ , where  $F(x)$  is the photon energy flux.

<sup>3</sup> Depending on the parameters the seed soft photons are either from the external medium or the synchrotron photons produced in the jet. In the first case, the inverse Compton (IC) scattered radiation is called the external radiation Compton (ERC) and in the second case, the synchrotron self-Compton (SSC).

<sup>1</sup> We use standard notations  $Q = 10^x Q_x$  in cgs units and for dimensionless variables.

## 2.2 Model of the jet

We consider a jet propagating from the centre of the quasar accretion disc of luminosity  $L_d$  through the external medium filled with the soft photons from the disc as well as scattered in the environment. The total jet power scales with the disc luminosity  $L_j = \eta_j L_d$ . The comoving value of the magnetic field in the jet  $B_j$  (its direction is transversal by assumption) is related to the Poynting flux carried by the (two-sided) jet

$$L_B = \eta_B L_j = \frac{B_j^2}{8\pi} 2\pi R_j^2 \Gamma_j^2 c \sim 8 \times 10^{43} B_j^2 R_{17}^2 (\theta \Gamma_j)^2 \text{ erg s}^{-1}, \quad (3)$$

which is assumed to be independent of distance (i.e. the magnetic field scales as  $B_j \propto 1/R$ ). The ratio of the Poynting flux to the total jet power  $\eta_B$  affects the ratio of synchrotron and Compton losses. The form of the rest of the energy content is not important in our approach as we ignore the internal pressure. We just assume that the jet does not contain high-energy interacting particles except those that are produced by the studied mechanism. If the rest of the jet energy is dominated by cold protons, the jet kinetic power (including the rest mass) is

$$L_k = (1 - \eta_B) L_j = \Gamma_j \dot{M} c^2 = 2\pi (R\theta)^2 \Gamma_j m_p c^3 n_p, \quad (4)$$

where  $\dot{M}$  is the mass outflow rate and  $n_p$  is the proton concentration (in lab frame). The total jet power is then  $L_j = L_k + L_B$ .

## 2.3 External environment

### 2.3.1 Accretion disc radiation

As discussed in SP06, the photon breeding mechanism requires the existence of the external soft radiation field which is opaque for high-energy photons against pair production. The emission of the accretion disc is opaque for high-energy ( $\sim 10^5$  MeV) photons moving across the jet up to the distance of a few parsec for the disc luminosity  $L_d \sim 10^{45}$  erg s $^{-1}$ . We characterise this radiation by the multicolour disc spectrum assuming a power-law  $T(\varpi) = T_{\max}(\varpi/\varpi_{\text{in}})^{-3/4}$  dependence of temperature on the disc radius  $\varpi$ , with the ratio of the outer to inner disc radius  $\varpi_{\text{out}}/\varpi_{\text{in}} = 10^4$ . Here  $T_{\max} = 5$  eV is the maximum disc temperature at  $\varpi_{\text{in}} = 3R_S$  and  $R_S = 2GM/c^2$  is the black hole Schwarzschild radius. The dimensionless maximal temperature is  $\Theta_{\max} \equiv kT_{\max}/m_e c^2 = 10^{-5}$ . We neglect the expected dependence on the luminosity  $T_{\max} \propto L_d^{1/4}$  as it is a small effect.

At distances much larger than the disc size, the disc radiation is directed along the jet and does not interact with the gamma-rays produced in the jet. Thus the conversion of these gamma-rays into electron-positron pairs requires a source of transversal soft photons. Below we consider three possibilities for such sources at different distance scales.

### 2.3.2 External radiation

- **Model A.** This model represents the isotropic radiation from the broad emission line region (BLR) at a subparsec distance  $R = 2 \cdot 10^{17}$  cm (as in SP06). The soft external radiation in this case is the disc radiation reprocessed and scattered by clouds in the BLR with an admixture of a softer infrared radiation from larger distances. The resulting spectrum has a complicated form, which we parametrize here (as in SP06) by a cutoff power-law  $F_{\text{BLR}}(x) \propto x^{-\alpha} \exp(-x/x_{\max})$  extending from the far-infrared  $x_{\min} \sim 10^{-9}$  to the UV band, as we assume  $x_{\max} = \Theta_{\max}$ . The normalization

of this spectrum is given by the parameter  $\eta_i \equiv U_{\text{iso}}/U_d$ , which defines the ratio of the energy density of the isotropic component to that of the direct disc radiation. We use  $\eta_i = 0.05$  in most of the simulations.

The results are sensitive to the spectral slope  $\alpha$  which describes the relative number of soft photons. Here we set  $\alpha = 0.4$  which implies that the ratio of the isotropic energy density in the IR range to that of the direct disc radiation is  $\sim 0.003$  (for  $\eta_i = 0.05$ ). Such IR contribution can be supplied by the dust at a parsec scale which can absorb and reemit in the IR range a substantial part of the quasar luminosity.

- **Model B.** It describes the radiation field at a few parsec scale, where the isotropic component is dominated by the infrared radiation of the dusty torus heated by the disc radiation. The isotropic component of the radiation field is represented as a blackbody with temperature  $T = 600$  K ( $\Theta = 10^{-7}$ ) and  $\eta_i = 0.1$  or  $0.3$ .

- **Model C.** No separate isotropic component is present. The radiation field is provided by the accretion disc only (Dermer & Schlickeiser 1993). At  $R \sim 10^{16}$  cm the angular size of the accretion disc is large enough to illuminate the jet under large angles. We take a standard multicolour disc, but for simplicity assume that there is one-to-one correspondence between the emitted photon energy  $x$  and the angle  $\phi$  between the jet direction and the photon momentum:

$$\tan \phi = \frac{\varpi}{R} = \frac{\varpi_{\text{in}}}{R} \left( \frac{x}{\Theta_{\max}} \right)^{-4/3}. \quad (5)$$

### 2.3.3 External matter

The external environment is kept at rest in spite of the fact that it gets a considerable momentum from photons producing pairs outside the jet. This momentum will cause an entrainment of the external medium which is not easy to simulate. It is important that this motion should be nonrelativistic, otherwise the gradient of the Lorentz factor would be significantly lower than that in the simulations. We discuss the quantitative condition for this in Section 4.3.

The magnetic field in the external medium is assumed to be of toroidal geometry with strength  $10^{-3}$  G.

## 2.4 Model parameters

The efficiency of the considered mechanism depends not directly on the luminosities, but on the dimensionless compactness parameters. The compactnesses of the radiation and of the magnetic field can be defined as

$$\ell = \frac{\sigma_T}{m_e c^2} U R_j, \quad (6)$$

where  $U$  is the corresponding energy density. The compactness is useful when estimating the cooling rate of pairs. The comoving magnetic compactness is defined as

$$\begin{aligned} \ell_B &= \frac{\sigma_T}{m_e c^2} \frac{B_j^2}{8\pi} R_j = 3.2 \cdot 10^{-4} B_j^2 R_{j,16} \\ &= 4.3 \cdot 10^{-3} L_{B,45} R_{j,16}^{-1} \left( \frac{\Gamma_j}{10} \right)^{-2}. \end{aligned} \quad (7)$$

The photon compactness, defined in the external frame, has two components: the direct accretion disc radiation

$$\ell_d = \frac{\sigma_T}{m_e c^2} \frac{2L_d}{4\pi R^2 c} R_j = 4.3 \cdot 10^{-3} L_{d,45} R_{17}^{-2} R_{j,16} \quad (8)$$

(with factor 2 in front of  $L_d$  coming from the Lambert law) and the isotropic component  $\ell_{\text{iso}} = \eta_i \ell_d$ . With these definitions, we can write the equation for electron energy losses in the jet frame (for model A) as

$$\frac{d\gamma}{dt'} \approx -(\ell_B + \ell_{\text{iso}}\Gamma_j^2 + \ell_d/\Gamma_j^2)\gamma^2, \quad (9)$$

where the term with  $\ell_B$  describes the synchrotron losses and the second and third terms – the Compton losses (in Thomson limit) on the isotropic radiation field (with a factor  $\sim \Gamma_j^2$  coming from the Lorentz transformation to the jet frame) and on the direct disc radiation, respectively. Because the soft photons can interact with high-energy pairs in Klein-Nishina regime, the second term in reality is much reduced. Equation (9) does not include SSC losses, which are zero at the beginning of the photon breeding cascade (because it takes time to build up the synchrotron energy density), but, in principle, can be significant at the steady-state regime. The pairs produced outside of the jet lose their energy mostly by Compton scattering of the disc radiation (the synchrotron losses are negligible because of the low magnetic field there) with  $\ell_d$  determining the cooling rate.

The jet compactness

$$\ell_j = \frac{\sigma_T}{m_e c^2} \frac{L_j}{2\pi R_j c} = 0.43 L_{j,45} R_{j,16}^{-1} \quad (10)$$

is related to the Thomson optical depth through the jet

$$\tau_p = \frac{m_e}{m_p} \frac{\ell_j}{\Gamma_j} (1 - \eta_B) = 2.3 \cdot 10^{-5} (1 - \eta_B) L_{j,45} R_{j,16}^{-1} \Gamma_{j,1}^{-1}. \quad (11)$$

## 2.5 Simulation method

### 2.5.1 Radiative processes

The numerical simulation of radiative processes is based on the Large Particle Monte-Carlo code (LPMC) described in Stern (1985) and Stern et al. (1995). The present version of the code handles Compton scattering, synchrotron radiation, photon-photon pair production, and pair annihilation. All these processes are reproduced without any simplifications at the micro-physics level. Synchrotron self-absorption was neglected as it consumes too much computing power and is not important at the considered conditions. The number of large particles (LPs) is  $2^{19} = 524288$  for most of the simulations. (in SP06 we used  $2^{17}$  LPs). The number of LP we use is still insufficient to completely get rid of numerical fluctuations. A substantially better resolution will require massive parallel computations and a smoothing technique which has to be developed.

### 2.5.2 Particle kinematics

The scheme of particle tracking in the relativistic fluid was developed in Stern (2003) and described in details in SP06. The 4-momentum of electron/positron LPs are defined in the jet frame. If the electron/positron has a critical Lorentz factor

$$\gamma_{\text{max}} \approx 10^8 B_j^{-1/2}, \quad (12)$$

it loses half of its energy in a half of Larmor orbit to synchrotron radiation. This requires a fine particle tracking at the first Larmor orbit if the comoving Lorentz factor of the particle is  $\gamma > \gamma_{\text{max}}$ , and, therefore, the comoving tracking step is limited by  $\Delta t' = 0.1 R_L/c$ , where  $R_L = 1.7 \cdot 10^3 \gamma/B_j$  cm is the Larmor radius.

When the particle energy is below  $\gamma_{\text{max}}$ , we neglect the dependence between the comoving direction and the energy and sample the direction of the particle assuming a uniform distribution of its gyration phase in the comoving system (see details in SP06).

The trajectories of electrons and positrons in the magnetic field are simulated directly assuming transversal geometry of the field in the jet as well as in the external matter.

### 2.5.3 Jet dynamics

Our model of the jet is the same as in SP06 except now we use 2D representation of the fluid instead of the 1D. We consider a piece of the jet centred at distance  $R$  from the central source and length  $20 R_j$ , where the jet radius is  $R_j = R\theta$  and  $\theta$  has the meaning of the opening angle, while for simplicity we approximate the jet by a cylinder of radius  $R_j$ . The boundary condition at the inlet (bottom of the cylinder) is the flow of constant Lorentz factor  $\Gamma_j$ . We introduce dimensionless coordinates, where the transversal distance from the jet axis is  $r$  and the distance from the central source  $z$  is measured in units of  $R_j$ . We use time unit of  $R_j/c$ . We use a fixed Eulerian grid with fairly rough spacing: 20 cells in the  $z$ -direction and 64 cells in the  $r$ -direction. The step on  $r$  is nonuniform: the spacing is finer near the jet boundary. The fluid in each cell  $i$  is characterised by its total energy  $E_i$  and momentum  $P_i$ , which define the Lorentz factor in the cell as

$$\Gamma_i = \frac{E_i}{\sqrt{E_i^2 - P_i^2}}. \quad (13)$$

The direction of the flow is treated as one-dimensional along the cylinder axis, because the transversal component of  $P_i^r$  never exceeds  $10^{-2}$  of the total momentum and the transversal displacement of the flow can be neglected.

### 2.5.4 Statistical representation

For a good statistical representation of the process, it is necessary to have more or less constant density of the LPs over the volume of the cylinder. As the energy (and number) density of particles (pairs and photons) grows by orders of magnitude from the inlet of the cylinder to the outlet, we need to introduce the dependence of statistical weights on  $z$ . The statistical weight  $w$  of a particle of energy  $\epsilon$  is defined through the energy content  $w\epsilon = 2^n s$ , where  $n$  is the integer part of  $z/2$  for  $z < 14$  and  $n = 7$  at  $z > 14$ . The value  $s$  varies with time in order to keep the total number of LPs within  $2^{19}$ . This weighting scheme is implemented as follows: we split a particle into two identical particles with twice less statistical weight when it crosses one of the planes  $z = 2, 4, 6, \dots$  in the direction opposite to the jet motion and we kill a particle with probability 0.5 and increase its weight by 2, when it crosses the plane in the direction of jet motion. The price for a good resolution at the region, where the avalanche starts and grows, is a poor resolution at the output. For that reason the Poisson noise in output light curves and photon spectra is rather high.

### 2.5.5 Simulation setup

At the start of simulations we set constant Lorentz factor  $\Gamma_j$  over the jet volume ( $r < 1$  and  $0 < z < 20$ , see Fig. 1) and assume a sharp boundary between the jet and the surrounding medium. We also inject a number of high-energy photons with the total energy several orders of magnitude smaller than the steady-state luminosity of the jet. (There is no injection of any additional photons later

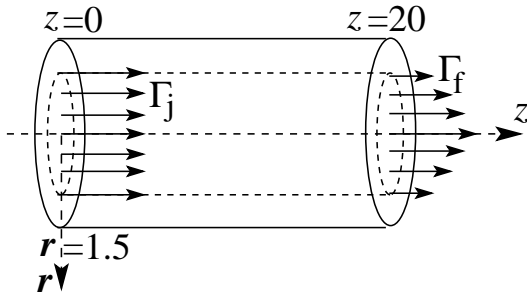


Figure 1. Geometry of the problem (not to scale).

during the simulations and the high-energy population of particles is self-supporting.) The external soft-photon radiation field is constant during the simulation.

Interactions between particles change the energy and momentum of the fluid. The electron-positron pairs born in the process become part of the fluid. The momentum and energy exchange between photons and each grid cell of the flow is accumulated during the time step  $\Delta t = 0.01 R_j/c$  and the total 4-momentum of the cell is updated after that. The momentum is transferred between cells along the jet axis.

The output of the simulations consists of the photons that escape from the cylindrical “simulation volume” with the boundaries  $r = 1.5, z = 20$ . We also record the energy spectrum of photons and pairs in the simulation volume.

### 3 RESULTS

#### 3.1 Simulation runs

We consider the distance scale of  $R \sim 10^{16}\text{--}10^{19}$  cm and the jet Lorentz factor  $\Gamma_j \sim 8\text{--}40$ . We vary the luminosity of the accretion disc  $L_d$  in the interval  $\sim 10^{43}\text{--}10^{46}$  erg s $^{-1}$  and try different ratios of the jet to the disc power. First, we present results of three series of simulations where we vary one of the parameters and nine non-systematic runs covering a wider area of parameters to demonstrate the working area of the mechanism. In the two series we vary the disc and jet luminosity, while in the third series we vary the jet Lorentz factor. Most of our simulation runs concern model A. Three runs correspond to different astrophysical scenarios described by models B and C, where the photon breeding operates.

(i) Runs 01–05. This series represents magnetically dominated jet (i.e.  $\eta_B = 1$ ) with the jet power equal to the disc luminosity ( $\eta_j = 1$ ), which is varied between  $L_d = 3 \cdot 10^{45}$  erg s $^{-1}$  down to  $3 \cdot 10^{43}$  erg s $^{-1}$ , where the photon breeding becomes sub-critical and the process does not work (at  $R = 2 \cdot 10^{17}$ ).

(ii) Runs 10–16. Similar to the previous series, but for the matter dominated jet with  $\eta_B = 0.2$  and  $\eta_j = 1$ . We vary  $L_d$  in a wider range, because the process for smaller  $\eta_B$  has a lower luminosity threshold.

(iii) Runs 21–25. In this series we have fixed the disc luminosity to  $L_d = 3 \cdot 10^{44}$  erg s $^{-1}$  use  $\eta_j = 1$  and  $\eta_B = 0.2$ , and vary the initial Lorentz factor of the jet.

(iv) Run 30 demonstrates a photon breeding process starting from the extragalactic gamma-ray background and resulting in 20 orders of magnitude growth of the high-energy photon population (see Sect. 4.5). Runs 31 represents a strongly non-linear system, where the jet power exceeds the disc luminosity. Run 32 is the case of the weakest AGN ( $L_d = 2 \cdot 10^{43}$  erg s $^{-1}$ ) tried in this work

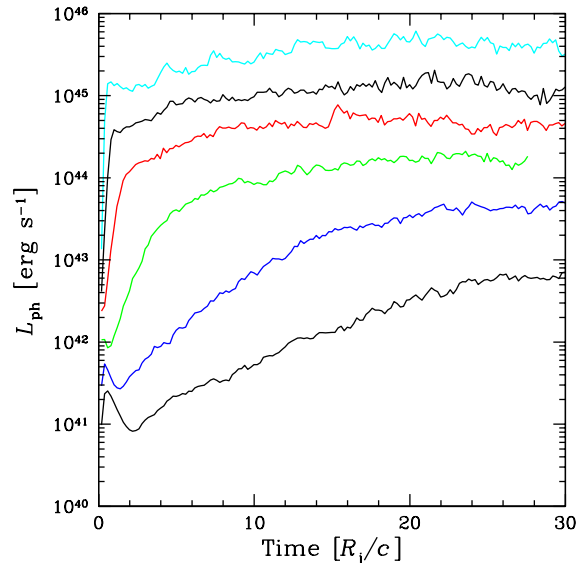


Figure 2. The power converted into photons (including those born in the jet, but not yet escaped) versus time for series of runs 10–15 (from top to bottom).

for model A. Run 33 demonstrates that a high efficiency can be achieved at  $\Gamma_j = 10$  if the magnetic field is weak. Run 34 is a trial with the lowest Lorentz factor,  $\Gamma_j = 8$ , and small Poynting flux. Run 35 is similar to run 12, but for the harder spectrum of isotropic external photons ( $\alpha = 0$  instead of  $\alpha = 0.4$ ).

(v) Runs 41–42 correspond to Model B, where we simulate interaction of a strong jet  $L_j = 2.3 \cdot 10^{45}$  erg s $^{-1}$  of Lorentz factor  $\Gamma_j = 20$  with the infrared radiation ( $\Theta = 10^{-7}$ ) of the dusty torus at a parsec scale. Run 43 describes Model C, where a relatively weak,  $\eta_j = 0.1$ , jet interacts with the direct radiation from the accretion disc of  $L_d = 8 \cdot 10^{43}$  erg s $^{-1}$  at a distance of a hundred gravitational radii (for a  $10^8$  solar mass black hole).

The parameters for these runs are summarised in Table 1.

#### 3.2 Time evolution and the steady-state regime

The energy release curves for set 2 (runs 10–15) are presented in Fig. 2. All curves show an exponential rise at the start with the time constant depending on the disc luminosity. The fast exponential rise turns to a slower growth when approaching the steady state. A very fast rise (time constant  $\sim 0.1 R_j/c$  for run 10) occurs in the case of a dense external radiation field when the photon free path length is much smaller than the jet radius. Then the photon breeding takes place only in a narrow layer at the jet boundary. Such fast breeding terminates after a short time, when the thin boundary layer decelerates. The breeding turns to a slower mode, where the softer photons with a longer free path dominate.

Note that the injection of external high-energy photons takes place only at the start of the simulation. Then the regime becomes self-supporting. The reason for this is a spatial feedback loop. The photon avalanche develops from a smaller to a large  $z$ , but some high-energy photons produced in the external environment move in the opposite direction, from larger  $z$ , where there are many high energy photons, to smaller  $z$ , where they can initiate a new photon avalanche. Due to this feedback a high efficiency of emission  $\varepsilon_{\text{eff}} = L_{\text{ph}}/L_j$  can be reached even if the growth of the photon avalanche is slow.

**Table 1.** Model parameters and results.

Run	$R^a$ cm	$\Gamma_j^b$	$\theta^c$	$L_d^d$ erg s $^{-1}$	ER $^e$	$\eta_i^f$	$\eta_j^g$	$\eta_B^h$	$\ell_d^i$	$\Gamma_j^2 \ell_{\text{iso}}^j$	$\ell_B^k$	$B^l$ G	$\tau_p^m$	$t_{\text{pb}}^n$	$\Gamma_f^o$	$\epsilon_{\text{eff}}^p$
01	2E17	20	0.05	3E45	A	0.05	1.0	1.0	3.3E-3	6.6E-2	3E-3	3.2	0	0.5	18.0	0.25
02	2E17	20	0.05	1E45	A	0.05	1.0	1.0	1.1E-3	2.2E-2	1E-3	1.8	0	1.1	18.0	0.32
03	2E17	20	0.05	3E44	A	0.05	1.0	1.0	3.3E-4	6.6E-3	3E-4	1.1	0	3.7	18.6	0.26
04	2E17	20	0.05	1E44	A	0.05	1.0	1.0	1.1E-4	2.2E-3	1E-4	0.6	0	6.2	19.6	0.05
05	2E17	20	0.05	3E43	A	0.05	1.0	1.0	3.3E-5	6.6E-4	3E-5	0.35	0	–	20.0	0
10	2E17	20	0.05	1E46	A	0.05	1.0	0.2	1.1E-2	2.2E-1	2E-3	2.6	9.3E-5	0.1	16.2	0.42
11	2E17	20	0.05	3E45	A	0.05	1.0	0.2	3.3E-3	6.6E-2	6E-4	1.4	2.8E-5	0.2	16.2	0.44
12	2E17	20	0.05	1E45	A	0.05	1.0	0.2	1.1E-3	2.2E-2	2E-4	0.82	9.3E-6	0.42	14.7	0.50
13	2E17	20	0.05	3E44	A	0.05	1.0	0.2	3.3E-4	6.6E-3	6E-5	0.45	2.8E-6	1.2	13.6	0.56
14	2E17	20	0.05	1E44	A	0.05	1.0	0.2	1.1E-4	2.2E-3	2E-5	0.26	9.3E-7	3.0	15.6	0.41
15	2E17	20	0.05	5E43	A	0.05	1.0	0.2	5.5E-5	1.1E-3	1E-5	0.18	4.6E-7	5.2	18.6	0.12
16	2E17	20	0.05	3E43	A	0.05	1.0	0.2	3.3E-5	6.6E-4	6E-6	0.14	2.8E-7	–	20.0	0
21	2E17	40	0.05	3E44	A	0.05	1.0	0.2	3.3E-4	2.6E-3	1.5E-5	0.22	1.4E-6	0.62	11.5	0.81
22	2E17	30	0.05	3E44	A	0.05	1.0	0.2	3.3E-4	1.5E-3	2.7E-5	0.30	1.8E-6	0.78	12.4	0.76
23=13	2E17	20	0.05	3E44	A	0.05	1.0	0.2	3.3E-4	6.6E-3	6E-5	0.45	2.8E-6	1.2	13.6	0.56
24	2E17	14	0.05	3E44	A	0.05	1.0	0.2	3.3E-4	3.2E-3	1.5E-4	0.71	3.9E-6	3.0	13.6	0.14
25	2E17	12	0.05	3E44	A	0.05	1.0	0.2	3.3E-4	2.4E-3	1.9E-4	0.80	4.6E-6	–	12.0	0
30	2E17	20	0.05	1E44	A	0.05	1.0	0.12	1E-4	2E-3	1.3E-5	0.2	1.0E-6	2.7	12.7	0.53
31	2E17	20	0.05	1E45	A	0.05	9.0	0.13	1E-3	2E-2	1.3E-3	2	9.0E-6	0.95	17.7	0.30
32	2E17	20	0.05	2E43	A	0.05	1.0	5E-3	2.3E-5	4E-4	1.3E-7	0.02	2.3E-8	7.0	19.5	0.03
33	2E17	10	0.05	3E44	A	0.05	0.8	1.3E-2	3E-4	1.5E-3	1.3E-5	0.2	5.9E-6	1.8	8.7	0.31
34	2E17	8	0.05	3E44	A	0.05	1.0	7E-3	3E-4	1E-3	1.3E-5	0.2	9.3E-6	2.6	7.7	0.13
35≈12	2E17	20	0.05	1E45	A $^q$	0.05	1.0	0.2	1.1E-3	2.2E-2	2E-4	0.82	9.3E-6	1.8	16.2	0.41
41	6E18	20	0.033	1.3E45	B	0.3	1.8	2E-2	3E-5	3.7E-3	2.6E-6	0.02	1.3E-6	5.4	18.0	0.21
42	6E18	20	0.033	1.3E45	B	0.1	1.8	6E-3	3E-5	1.2E-3	6.4E-7	0.01	1.3E-6	6.3	19.1	0.14
43	6E15	20	0.067	8E43	C	0	1.0	6E-2	4E-3	0	1.3E-5	1.0	2.2E-6	2.3	19.2	0.19

$^a$ Distance from the black hole.  $^b$ Initial Lorentz factor of the jet.  $^c$ Half-opening angle of the jet.  $^d$ Total disc luminosity.  $^e$ Model of the external radiation described in Section 2.3.2.  $^f$ Ratio of the isotropic soft photon energy density to that of the disc.  $^g$ Ratio of the total jet power to the disc luminosity,  $L_j/L_d$ .  $^h$ Fraction of the jet power carried by the Poynting flux,  $L_B/L_j$ .  $^i$ Disk compactness.  $^j$ Compactness of the isotropic external radiation in the jet frame.  $^k$ Magnetic compactness.  $^l$ Magnetic field in the jet.  $^m$ Thomson optical depth through the jet produced by electrons associated with protons.  $^n$ e-folding time of the photon breeding in  $R_j/c$  units.  $^o$ Terminal Lorentz factor at the jet axis.  $^p$ Average efficiency of the jet energy conversion into radiation at the steady-state.  $^q$ Modified model A with a harder spectrum of external isotropic photons ( $\alpha = 0$ ).

We can see large fluctuations of the energy release at the saturation regime (at the stage of the exponential rise, the curves are smooth). Fluctuations have the Poisson component which is large because of the weighting method: LPs at the outlet have statistical weight  $2^7$  larger than at the inlet. There are also non-Poisson fluctuation which are caused by fluctuations in the spatial feedback: a photon with a large statistical weight moves from the end of the active jet fragment to its beginning, interacts there and produces a photon avalanche. The number of such photons is small, but the amplification coefficient (i.e. the number of secondary photons and pairs) can exceed  $10^4$ . Therefore the number of LPs as large as  $\sim 10^6$  is still insufficient for a good statistical representation.

However, statistical noise is not the only reason for the large fluctuations in the output photon flux. In runs 10 and 31, where the compactness is high, and especially in run 31, where the system is strongly non-linear, we see a large amplitude variability at a range of time-scales (see Fig. 3). We performed run 31 with the different number of LPs:  $2^{19}$  and  $2^{21}$ , but the character and the amplitude of the fluctuations was similar. Thus, in this case we deal with the real instability of a non-linear dynamical system (see Sect. 4.2 for discussion).

### 3.3 Radiative efficiency and the “working area” of the process

The resulting efficiency of the conversion of jet power into radiation at the steady-state and the time constant of the exponential photon breeding are shown in the last columns of Table 1. Once we fixed  $R$ ,  $R_j$ , and the ratio  $\eta_i$  in all runs for model A, our main remaining parameters are the jet Lorentz factor, the disc luminosity and the Poynting flux. The jet power is not important unless it exceeds the disc luminosity (as in run 31), making the system strongly non-linear. The series of runs 01–05 shows that the process can work efficiently in the case of a magnetically dominated jet giving  $\epsilon_{\text{eff}} \approx 1/4$ . The lowest luminosity when it works is  $\sim 10^{44}$  erg s $^{-1}$ . If the matter dominates over the magnetic energy by a factor of 5 (runs 10–16) then the radiative efficiency is higher, above 50 per cent, and the working luminosity range slightly extends down to  $5 \cdot 10^{43}$  erg s $^{-1}$ . The supercritical breeding is still possible at even lower disc luminosity,  $2 \cdot 10^{43}$  erg s $^{-1}$  (see run 32), but only if the magnetic field is very weak. Below this threshold the photon-photon opacity across the jet (see Eq. 2) becomes insufficient. (We note here that the working luminosity limits are given for  $R = 2 \cdot 10^{17}$  cm,  $\Gamma_j = 20$  and  $\eta_i = 0.05$ .)

Remarkably, the efficiency at a moderate disc luminosity ( $\sim$

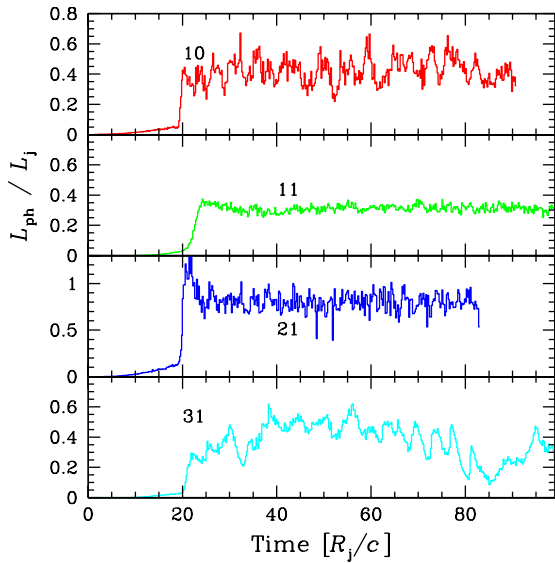


**Figure 3.** The escaping photon luminosity in units of the jet power versus time for runs 10, 11, 21 and 31. Note that the light curves look different compared to Fig. 2 as it takes about 20 time units for photons to escape from the simulation cylinder (and the ordinate scale is linear here).

$3 \cdot 10^{44} \text{ erg s}^{-1}$ , run 13) is higher than for a more luminous quasar (runs 10, 11 and 31). The reason is that at a high luminosity the spine of the jet is shielded from the high-energy external photons by the opaque (respectively to pair production) radiation of the accretion disc and synchrotron radiation of pairs in the jet. In runs 10 and 31, only the photons with energy  $\epsilon < 10^3$  can penetrate deeply into the jet. Nevertheless, such moderate energy photons still can interact with the synchrotron photons (mostly produced in the decelerated outer jet layers) inside the jet and support the photon breeding.

As one can expect, the dependence on  $\Gamma_j$  is very strong. The efficiency  $\varepsilon_{\text{eff}}$  is close to  $(\Gamma_j - \overline{\Gamma_f})/\Gamma_j$ , where the average Lorentz factor at the outlet  $\overline{\Gamma_f}$  slightly *decreases* when  $\Gamma_j$  increases (see Sect. 3.4).

At a lower  $\Gamma_j$  the process becomes very sensitive to the ratio of the Poynting flux to the isotropic disc luminosity. Indeed, at the given magnetic flux  $L_B$  the comoving magnetic compactness scales as  $\ell_B \propto L_B/\Gamma_j^2$  (see Eqs. 7), while Compton cooling rate in the Thomson limit scales as  $\propto \ell_{\text{iso}}\Gamma_j^2$ , see Eq. (9). Thus the ratio of Compton to synchrotron losses scales as (see e.g. SP06):

$$\frac{U'_{\text{iso}}}{U_B} = \frac{\eta_i}{\eta_B} \Gamma_j^4 \theta^2. \quad (14)$$

This ratio decreases somewhat because of the Klein-Nishina effect, but it is still a strong function on  $\Gamma_j$ . That is the reason why the runaway photon breeding does not happen at  $\Gamma_j < 14$  if  $\eta_B = 0.2$  (series 21–25). If the magnetic field is very weak, then the process can work efficiently at  $\Gamma_j = 10$  (run 33) and less efficiently, but still in a self-supporting regime at  $\Gamma_j = 8$  (run 34).

All results described above are obtained under an assumption that the BLR is relatively abundant with isotropic infrared photons, so that the photon spectrum can be roughly approximated as a cut-off powerlaw with  $\alpha = 0.4$  (see Sect. 2.3.2). The spectrum however can be harder if, for example, there is no sufficient amount of dust around the AGN. Therefore, we made a couple of trials for model A with a harder BLR spectrum,  $\alpha = 0$ . One trials with the same parameters as run 13 ( $L_d = L_j = 3 \cdot 10^{44} \text{ erg s}^{-1}$ )

resulted in no self-supporting photon breeding. Another trial with ( $L_d = L_j = 10^{45} \text{ erg s}^{-1}$  (run 35 in Table 1) demonstrated photon breeding, which was slower than in run 12 (with  $\alpha = 0.4$ ). However, the final steady state was almost the same including the radiative efficiency (0.41 versus 0.5 in run 12) and the emitted spectrum. Such a striking difference between the two cases differing only by factor 3 in luminosity appears because of the non-linear character of the mechanism for high-power jets: soft synchrotron photons produced by the jet significantly contribute to the photon-photon opacity. The problem with soft photon starvation can be overpassed if some internal jet activity (e.g. internal shocks) supply soft synchrotron photons which can be then scattered in the BLR (Ghisellini & Madau 1996).

In general, the results of our simulations for distance  $R$  from the black hole and luminosity  $L$ , can be scaled to another distance  $R'$  if one changes at the same time all luminosities as  $L' = LR'/R$ . In this case, the compactnesses of all radiation components and of the magnetic energy do not change (see Eq. 6). Such scaling is not exact, because the value of magnetic field changes and the synchrotron spectra change accordingly. The scaling, however, does not affect the criticality of the system as long as the ratio between synchrotron and Compton losses remain constant.

At luminosity smaller than about  $L_{d,\text{min}} \approx 10^{43} R_{17} \text{ erg s}^{-1}$  the opacity for pair-production through the jet becomes smaller than unity and the super-criticality condition breaks down. Assuming the distance to the emission region of  $R \sim 10^3 R_S$ , we can express the luminosity threshold in terms of the Eddington luminosity  $L_{d,\text{min}} \sim 10^{-5} L_{\text{Edd}}$  which is quite moderate.

The distance to the BLR may also depend on the luminosity of the object. The reverberation mapping gives the relation  $R_{\text{BLR},17} \approx L_{d,44}^{1/2}$  (Peterson 1993; Kaspi et al. 2005). This then gives the condition  $L_{d,44} > 0.1 L_{d,44}^{1/2}$ , which translates to the lower limit on the luminosity  $L_d > 10^{42} \text{ erg s}^{-1}$ , when the photon breeding can operate.

The conditions when model A operates can be summarised as follows:

- At  $\Gamma_j \gtrsim 20$  and at  $L_{d,44} \sim L_{j,44} \gtrsim 5R_{17}$  the photon breeding mechanism is efficient and very robust: it works independently on the share of magnetic energy in the jet and is not sensitive to the spectrum of the external radiation.
- At  $\Gamma_j \gtrsim 20$  and lower jet power  $L_{j,44} < 5R_{17}$ , when the disc luminosity is still sufficiently high,  $L_{d,44} > 0.5R_{17}$ , the mechanism is sensitive to the spectrum of isotropic radiation in the BLR and, if there is a deficit of soft photons, the photon breeding is not self-supporting.
- For  $\Gamma_j < 20$  the mechanism becomes sensitive to the magnetic field in the jet. The strong field inhibits the photon breeding. When the magnetic energy is much smaller than the matter kinetic energy, the efficient emission is possible down to  $\Gamma_j \approx 8$ .
- The threshold of the disc luminosity is  $L_{d,44} \sim 0.1R_{17}$ . However, the self-supporting emission at such low  $L_d$  requires weak magnetic field and a soft spectrum of the BLR radiation.

We also have tried models B and C with a couple of runs for each just to show that the process can work in different situations. Radiative efficiencies of 20 per cent are easily reached. We do not perform a systematic study of these models because both scenarios depend on various conditions that require a different study. Model C, for example, should be considered together with the mechanism of the jet launching and in model B one should account for the history of the jet flow before it reaches the parsec-scale distance.

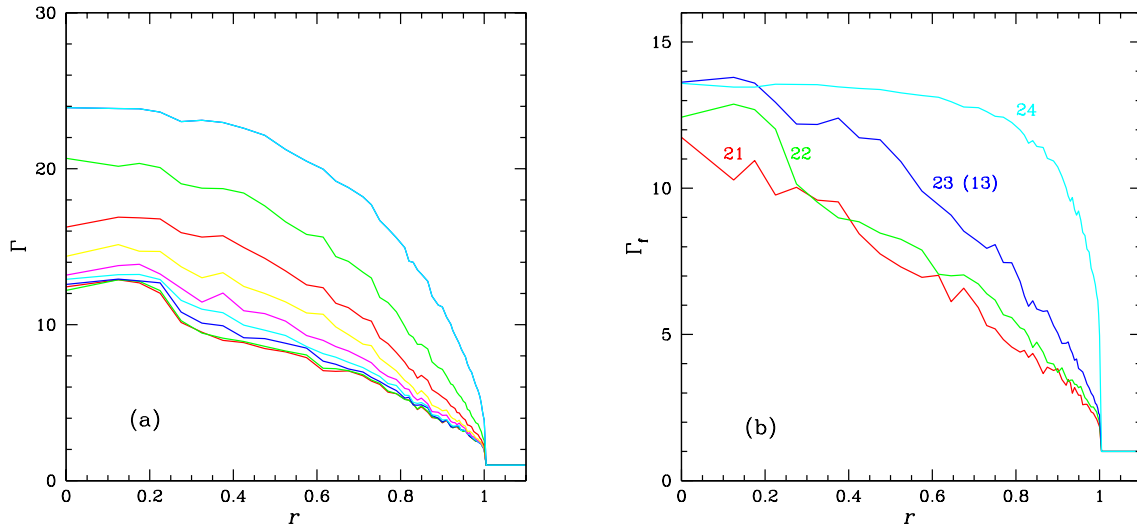


**Figure 4.** The transversal distribution of the bulk Lorentz factor. (a) Dependence on distance  $z$  for run 22 (curves from top to bottom correspond to  $z = 20$  with step 2 till  $z = 2$ ). (b) Distribution of the terminal Lorentz factor at the outlet ( $z = 20$ ) for runs 21–24.

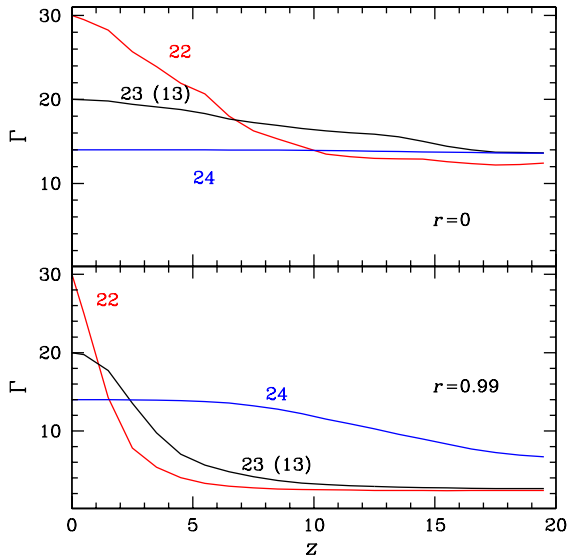


**Figure 5.** Distribution of the fluid Lorentz factor in  $z$  direction for runs 22–24. Upper panel shows the Lorentz factor at the jet axis  $r = 0$ , lower panel – near the jet boundary at  $r = 0.99$ .

### 3.4 Jet deceleration and the energy release

Jet deceleration in the 1D approach of SP06 took place mainly near the jet boundary ( $r > 0.9$ ), while the centre of the jet was not affected. In the 2D simulations we can track the deceleration of the deeper parts of the jet up to its axis. The transversal distributions of the fluid Lorentz factor for runs 21–24 are shown in Fig. 4. Distributions of  $\Gamma$  along the jet axis are shown in Fig. 5. It is remarkable that the terminal Lorentz factor  $\Gamma_f$  depends weakly on the initial  $\Gamma_j$ , actually it even decreases when  $\Gamma_j$  increases.

The highest gradient of the Lorentz factor is near the jet boundary. In the case of run 22, the Lorentz factor near the boundary drops from 30 down to 5 at  $z = 3$  (see Fig. 5). The jet experienced similar deceleration in runs 01, 10, 11 and 31, where the radiation density is high. At the outlet the transversal gradient of  $\Gamma_f$  almost

does not depend on distance from the axis. It reaches some critical value beyond which the photon breeding is not effective anymore. In cases of a lower compactness (runs 04, 14, 15, 32) the Lorentz factor changes more smoothly with  $z$ . At the outlet,  $d\Gamma/dr$  is still large close to the boundary, with the jet getting the form of a fast spine and a slow sheath. Large radial gradient of  $\Gamma$  means that our ballistic approximation rapidly breaks down in the cases of a large compactness or a large initial Lorentz factor. We discuss a number of important effects, which are missed in our simulations in Section 4.4.

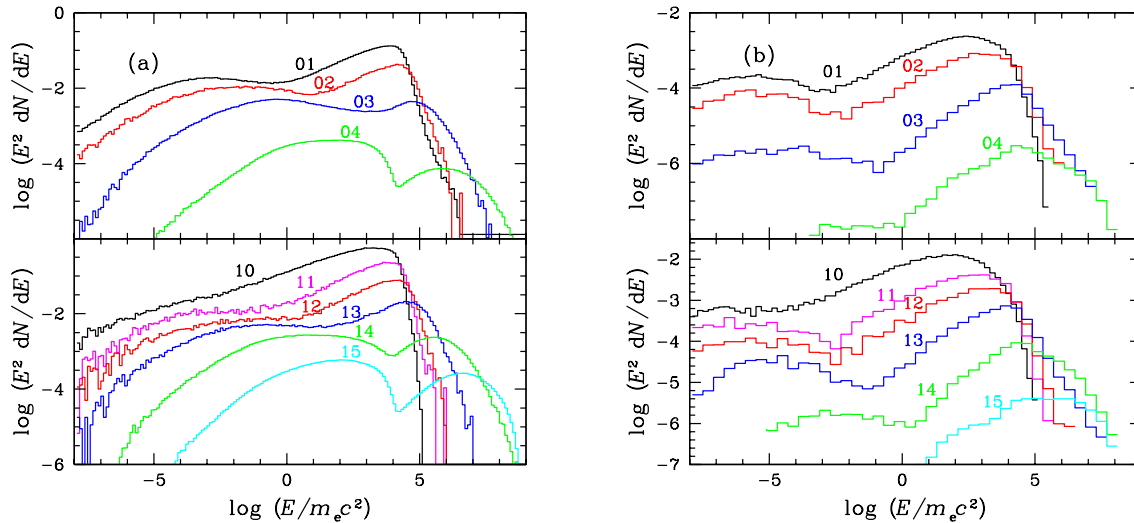
### 3.5 Radiation spectra

Figure 6(a) shows the output spectra of photons emitted in the direction of the jet ( $\theta < 10^\circ$ ). Spectra (except those for runs 10 and 31 with very high compactness) show a two-component synchrotron - Compton structure. Runs 01–03 produce a synchrotron peak in the range  $\epsilon \sim 10^{-3} - 10^{-1}$ , consistent with those observed in BL Lacs, however, the theoretical peaks are less prominent than the observed ones (detailed comparison with the observed spectra is presented in section 5.1), partially due to averaging over angles. The Compton components at high  $L_d$  and  $L_j$  (runs 01, 02, 10–12, 31) have a cutoff at  $10^4 < \epsilon < 10^5$  due to the photon-photon absorption: the external isotropic BLR radiation provides a larger than unity optical depth for high-energy photons.

Spectra for a smaller compactness (runs 04, 14, 15, 32, as well as runs 41, 42, where the compactness is small because of large  $R$ ), have prominent synchrotron peaks at high energies  $\epsilon \sim 10^0 - 10^3$ . The synchrotron and Compton components are clearly separated at  $\epsilon \sim 10^4$ , the maximal energy of synchrotron radiation:

$$\epsilon_{s,\max} \sim \Gamma_j^2 \gamma_{\max}^2 B_j / B_{\text{QED}} \approx 230 \Gamma_j, \quad (15)$$

which does not depend on magnetic field (here  $B_{\text{QED}} = 4.4 \cdot 10^{13}$  G is the critical QED field). The value of  $\gamma_{\max}$  given by equation (12) is defined as the maximal electron energy (in the jet frame) after half the Larmor orbit, i.e. when it turns around from the counter-jet direction to the jet propagation direction is (see SP06). The derived  $\epsilon_{s,\max}$  assumes that the magnetic field is uniform at the scale



**Figure 6.** Spectra of the escaping photons (angle-integrated) for runs 01–04 (upper panel) and runs 11–15 (lower panel). (a) Radiation spectra emitted along the jet axis with  $\theta < 10^\circ$ . (b) Radiation spectra at large angles to the jet axis,  $\theta > 40^\circ$ .

of the electron Larmor radius and transversal to the jet. It is not sensitive to the soft radiation field because an electron with the comoving frame Lorentz factor  $\gamma \gtrsim 10^8$  interacts with the external radiation in the deep Klein-Nishina regime and the synchrotron losses dominate. Thus, the model predicts a new spectral feature which, in principle, can be observed by *GLAST*. Its detection would be a clear signature of the photon breeding mechanism (a distribution of diffusively accelerated electrons will hardly extend to the energy when an electron loses a large fraction of its energy at one Larmor orbit). Moreover, because of independence of  $\epsilon_{s,\max}$  of the magnetic field and other parameters, the Lorentz factor of the jet can, in principle, be determined from the detailed fits of the shape of the spectral cutoff.

For the considered model parameters, the dominant source of seed soft photon for Compton scattering is BLR. At the start of simulations, the SSC losses are small, because the synchrotron energy density needs to be built up from zero. In the steady-state regime, the ratio of SSC losses to the synchrotron losses can be expressed as  $\epsilon_{\text{eff}} \eta_{s,\text{KN}} / \eta_{\text{B}}$ , where  $\eta_{s,\text{KN}}$  is the fraction of *soft* synchrotron radiation (i.e. Comptonized in Thomson regime) in the total jet luminosity. We can estimate from Fig. 6(a) that  $\eta_{s,\text{KN}} < 0.3$  for runs 01–03 (with  $\eta_{\text{B}} = 1$ ) and  $\eta_{s,\text{KN}} < 0.1$  for runs 10–12 (with  $\eta_{\text{B}} = 0.2$ ). For a lower jet and disc luminosity (runs 03–04, 13–15), the electrons in the jet have higher energies and the SSC losses are suppressed by the Klein-Nishina effect. Therefore SSC losses are always at least a few times smaller than the synchrotron losses and usually are much smaller than the ERC losses. However, the Compton losses of pairs in the fast spine of the jet on synchrotron photons originating from the slower sheath can be considerable, at least in runs 10 and 31 with the highest compactness. These cases can be considered as intermediate between SSC and ERC.

Spectra of radiation emitted at large angles relative to the jet axis are shown in Fig. 6(b). We again see two-component, synchrotron and Compton spectra. The total (angle-integrated) luminosity in the gamma-rays emitted at large angles to the jet axis is about two order of magnitude smaller than that of the beamed emission, which approximately corresponds to the gain factor  $\Gamma_j^2$ . The radiation spectra emitted as a function of the angle  $\theta$  between the line of sight and the jet axis are shown in Fig. 7. We see that

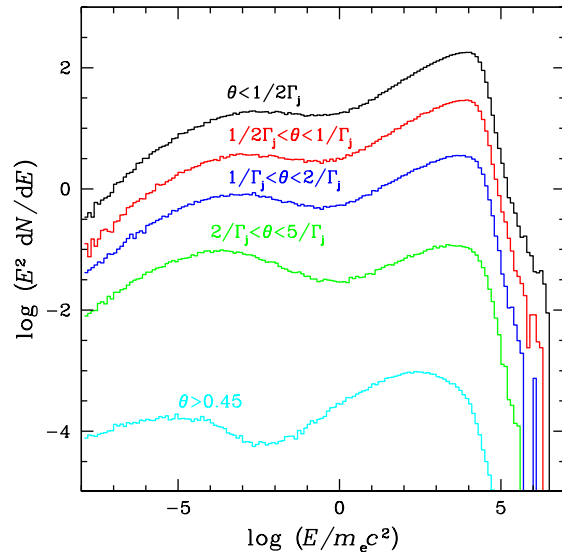


**Figure 7.** Intensity of radiation (per unit solid angle) at different angles to the jet axis for run 01.

the synchrotron peaks shift to lower energies for larger angle and therefore the two components are better separated.

### 3.6 Angular distributions of radiation

#### 3.6.1 Radiation from isotropic pairs in the steady jet

Let us first discuss what kind of angular distributions can be expected from a steady (narrow) axisymmetric jet in relativistic motion. In general the observed bolometric luminosity is related to the emitted one by the relation (see e.g. Lind & Blandford 1985; Sikora et al. 1997)

$$L(\theta) \equiv \frac{dL}{d\Omega} = \frac{\delta^3 dL'}{\Gamma_j d\Omega'} \quad (16)$$

where  $\delta = 1/\Gamma_j(1 - \beta_j \cos \theta)$  is the Doppler factor, and  $d\Omega = d\phi d\cos \theta$ . Let us define the amplification factor as a ratio of the observed and emitted luminosities

$$A(\theta) \equiv \frac{L(\theta)}{L'/4\pi}. \quad (17)$$

If the radiation source is isotropic in the jet frame, then  $dL'/d\Omega' = L'/4\pi$ , and

$$A(\theta) = \frac{\delta^3}{\Gamma_j}. \quad (18)$$

Integrating over the  $4\pi$ , we can verify that the total emitted and observed powers are the same. Equation (18) can be applied, for example, to the synchrotron radiation in tangled magnetic field or to the SSC radiation by isotropic electrons.

If soft photons are isotropic in the external medium, they are strongly beamed in the direction opposite to jet propagation in the jet frame. This results in the angular distribution of the radiation IC scattered by relativistic isotropic electrons (see e.g. Rybicki & Lightman 1979)

$$\frac{dL'}{d\Omega'} = \frac{L'}{4\pi} \frac{3}{4} (1 + \cos \theta')^2, \quad (19)$$

with  $\theta'$  being the angle to the direction of jet propagation. For small  $\theta$ , we can rewrite  $1 + \cos \theta' \approx \delta/\Gamma$ , and we get a much sharper angular dependence of the ERC radiation (see also Dermer 1995, and Fig. 8):

$$A(\theta) = \frac{3}{4} \frac{\delta^5}{\Gamma_j^3}. \quad (20)$$

Now the integration over all solid angles shows that the total observed power is 3/2 larger than the emitted one, which results from the non-zero net momentum of the emitted radiation in the jet co-moving frame (19).

### 3.6.2 Radiation of primary pairs

In the above we assumed explicitly an isotropic electron distribution. However, if the jet magnetic field has a toroidal geometry (as assumed in this paper), the distribution may significantly deviate from the isotropic one. For example, the first generation of pairs, produced in the jet by the external high-energy photons (which are beamed in the jet frame similarly to the external soft photons), has a very narrow distribution of pitch angles around  $\pi/2$ . Let us now derive the angular distribution of radiation expected from these ‘‘2D’’ pairs.

The pairs gyrating in a toroidal magnetic field have a flat distribution in  $\theta$  (not  $\cos \theta$ ). Therefore, their synchrotron emission has a pattern

$$\frac{dL'}{d\cos \theta'} = \frac{L'}{4\pi} \frac{1}{\pi} \frac{1}{\sin \theta'}. \quad (21)$$

An identical distribution would be produced by SSC emission (because the synchrotron photons that are Comptonized are mostly produced by the next generation, lower energy, isotropic pairs). With the relation  $\sin \theta' = \delta \sin \theta$ , we get the amplification factor (see dashed curves in Fig. 8)

$$A(\theta) = \frac{1}{\pi} \frac{\delta^2}{\Gamma_j} \frac{1}{\sin \theta}. \quad (22)$$

This distribution has sharp peaks at  $\theta = 0$  and  $\pi$ .

The external radiation IC scattered on 2D pairs produces a pattern

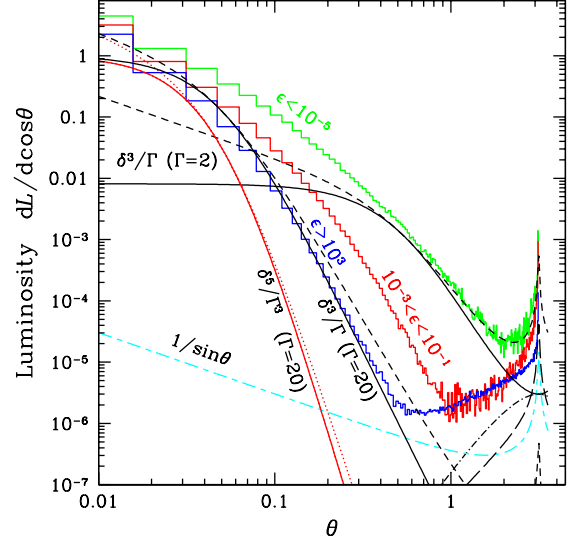


**Figure 8.** Luminosity (per unit solid angle) as a function of angle between the light of sight and the jet axis for run 01 in the three energy bands: IR-optical ( $\epsilon < 10^{-5}$ ), X-rays ( $10^{-3} < \epsilon < 10^{-1}$ ) and GeV gamma-rays ( $\epsilon > 10^3$ ) (histograms, arbitrary normalization). The theoretical dependencies (18) expected for the steady relativistic jet emitting isotropically in the comoving frame shown by solid (black) curves (cases with  $\Gamma = 2$  and 20). Dashed curves represent the synchrotron and SSC emission from pairs in 2D circular motion (in the plane containing the jet axis), given by equation (22). The solid (red) curve describes the jet ERC radiation from isotropic pairs (eq. 20), while the dotted (red) curve is for the jet ERC radiation from 2D pairs (eq. 24). The dot-dashed curve represents the emission of isotropic pairs in the external medium Comptonizing radiation beamed along the jet (eq. 27). The emission from 2D pairs in the external medium is shown by long dashes (IC of beamed emission, see eq. 26) and short-long dashes (synchrotron as well as IC of the isotropic photons, see eq. 25).

$$\frac{dL'}{d\cos \theta'} = \frac{L'}{4\pi} \frac{2}{3\pi} \frac{(1 + \cos \theta')^2}{\sin \theta'}, \quad (23)$$

which produces the distribution of the observed emission with the peaks at  $\theta = 0, \pi$  (see dotted curve in Fig. 8):

$$A(\theta) = \frac{2}{3\pi} \frac{\delta^4}{\Gamma_j^3} \frac{1}{\sin \theta}. \quad (24)$$

### 3.6.3 Radiation from external environment

In addition to the radiation from the jet, there is also radiation from the relativistic pairs produced in the external environment. They also have two populations. The first population is produced by the high-energy photons from the jet propagating a small angles to the jet direction  $\theta \lesssim 1/\Gamma$ . They perform 2D circular motion in the toroidal magnetic field of the surrounding. The second population produced by the pair cascade is nearly isotropic.

The synchrotron radiation of 2D pairs follows distribution (21), with  $\theta'$  replaced by  $\theta$  (see short-long dashes in Fig. 8).

$$L(\theta) \propto \frac{1}{\pi} \frac{1}{\sin \theta}. \quad (25)$$

The IC scattered isotropic BLR photons have the same distribution.

However, because most of the seed photons (synchrotron photons from the jet or the accretion disc photons) are beamed in the direction of the jet, the IC emission by the external pairs follows

the distribution (23) with  $\theta'$  replaced by  $\pi - \theta$  (see long dashes in Fig. 8):

$$L(\theta) \propto \frac{2}{3\pi} \frac{(1 - \cos \theta)^2}{\sin \theta}. \quad (26)$$

Thus, the 2D pairs produce a sharp peak at  $\theta = \pi$ .

The emission of isotropic pairs Comptonizing the disc (or jet synchrotron) radiation follows the law (19) with  $\theta'$  replaced by  $\pi - \theta$  (see dot-dashed curve in Fig. 8):

$$L(\theta) \propto \frac{3}{4} (1 - \cos \theta)^2. \quad (27)$$

And, finally, isotropic pairs scattering isotropic radiation obviously produce a flat distribution of  $L(\theta)$ .

### 3.6.4 Emission pattern: simulations

As an example of the angular distribution of radiation predicted by the photon breeding model, we present results for run 01. The histograms in Fig. 8 show the dependence of the luminosity in three typical energy bands (IR-optical, X-ray and gamma-rays). We see that the distribution of high-energy photons at small  $\theta$  follows quite closely that expected from the jet of  $\Gamma_j = 20$  emitting isotropically in its rest frame (e.g. SSC, given by eq. 18). The ERC radiation from the jet is more beamed (see eq. 20 and the red solid curve in Fig. 8). An excess at  $\theta = 0$  can be explained by the contribution of the SSC and ERC emission from 2D pairs (given by eqs. 22 and 24, respectively; see dashed and dotted curve in Fig. 8).

At angles  $\theta \gtrsim 0.45$ , another component is obvious. This large-angle component is nearly isotropic and its flux at infinity is 4.5 orders of magnitude smaller than the average flux observed within the jet opening. For the run 01 with  $\Gamma_j = 20$ , the observed luminosity of this large-angle component at  $\theta = \pi/2$  exceeds the luminosity given by expression (18) by more than 3 orders of magnitude. This off-axis emission is produced by the pairs gyrating in the external environment via Compton scattering of the disc and BLR photons and synchrotron photons from the jet. A peak at  $\theta = \pi$  can be well described by IC emission of 2D pairs in the external environment (see long dashes and short-long dashes in Fig. 8) given by formulae (25) and (26).

The low-energy (IR-optical and the X-rays) photons are much less beamed. The spatial gradients of  $\Gamma$  is the main cause of that. For example, the average  $\Gamma$  of the inner half of the jet volume with  $r < 0.7$  in run 01 is about 18, while the outer 20 per cent move with  $\Gamma \lesssim 10$ , dropping to  $\Gamma \sim 2$  in the outer 5 per cent (see also Figs 4 and 5).

The soft band is dominated by the synchrotron radiation (Fig. 7). The emission at  $\theta = 0.5$  exceeds the simple estimate (18) by 3 orders of magnitude. At angles  $\theta \gtrsim 1/\Gamma_j = 0.05$  the emission is mostly produced in the slower, decelerated layers of the jet (see Fig. 4), and the emission at  $\theta \gtrsim 0.5$  is produced in the layers of  $\Gamma \sim 2$ . The synchrotron from 2D pairs in the jet even produces a peak at  $\theta = \pi$ . Some contribution to this peak is provided by the IC (low-energy tail) emission from the external medium.

The emission in the X-rays is the mixture of the synchrotron and ERC emission resulting in the intermediate behaviour seen in Fig. 8. The large-angle emission here is produced by IC in the external environment (see Fig. 7) and therefore has an angular dependence similar to that of the gamma-rays.

The sharp feature at  $\theta = 0$  will be washed out if the jet is actually conical rather than cylindrical or the jet magnetic field is tangled. The tangled magnetic field in the external medium will also smooth out the predicted peak at  $\theta = \pi$ .

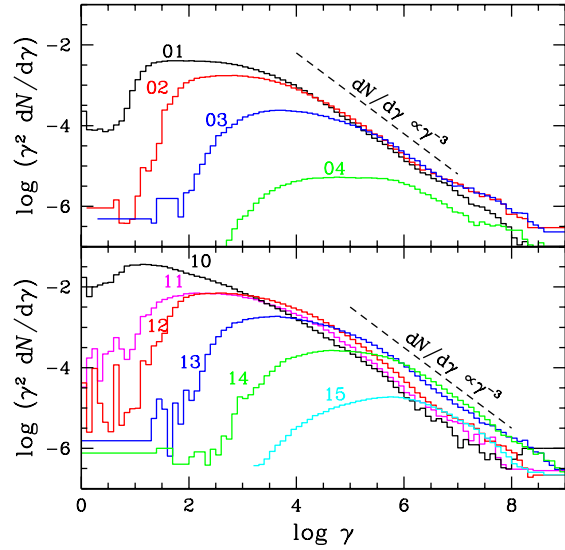


**Figure 9.** Electron (and positron) energy distributions in the jet comoving frame averaged over the jet volume.

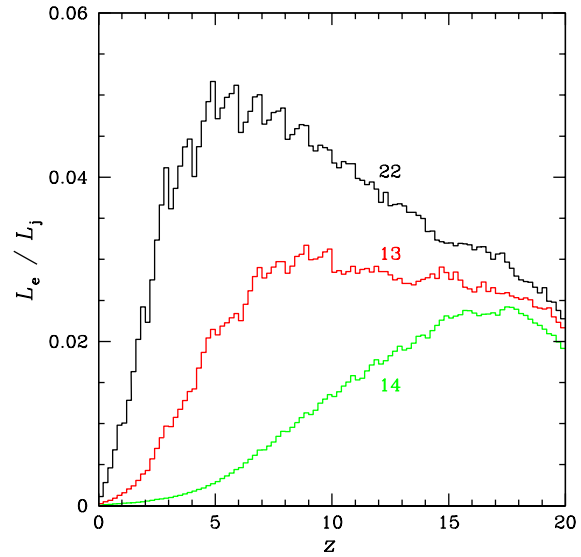


**Figure 10.** Kinetic luminosity carried by pairs with respect to the initial jet power. Periodic fluctuations for runs 13 and 22 are the artefacts of a rough spatial grid resulting in discreteness of the Lorentz factor.

## 3.7 Pairs produced in the jet

The electron and positron comoving energy distributions averaged over time and jet volume for runs 01–04 and 10–15 are shown in Fig. 9. All spectra except that for run 15 have a clear low-energy cutoff at  $\gamma_c = 10\text{--}10^3$ , this is the energy the pairs cool down to in the dynamical time. The cutoff comoving energy assuming the Thomson regime for Compton cooling and neglecting SSC can be expressed as

$$\gamma_c = \frac{1}{t'_{\text{dyn}} (\ell_B + \ell_{\text{iso}} \Gamma^2)}, \quad (28)$$

where  $t'_{\text{dyn}} \approx 10/\Gamma \sim 1$  is a typical (dimensionless) time the particles spend in the active cylinder. In our examples the Compton

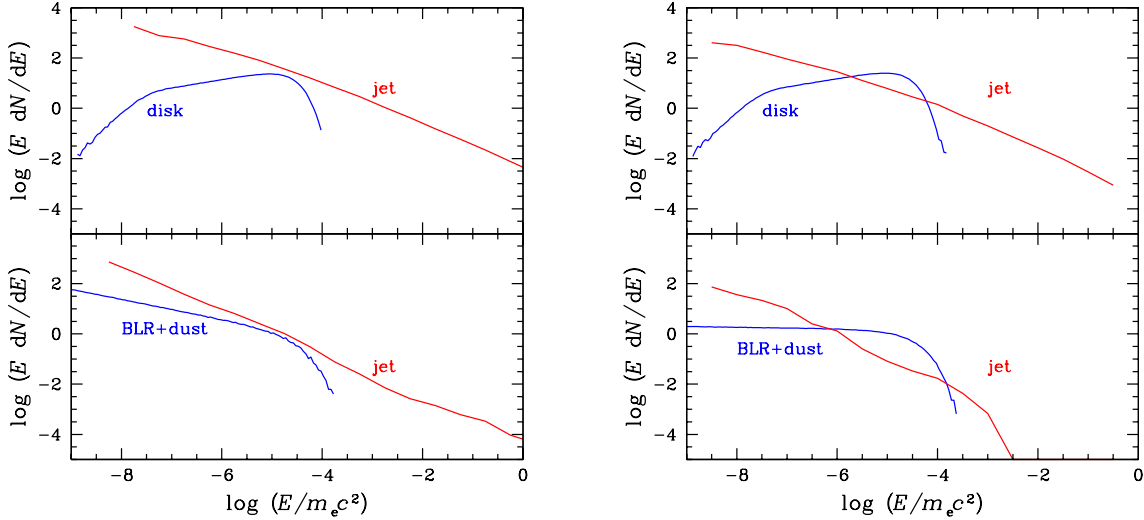


**Figure 11.** The spectra of the external radiation and of the soft (mostly synchrotron) radiation induced by the jet activity for run 31 (left) and run 35 (right). Notice that the spectra here are  $E dN/dE$ , not  $E^2 dN/dE$ , to emphasise the number density of target soft photons available for pair production. Upper panels: the collimated components, lower panels: the isotropic external radiation and the large-angle ( $\theta > 40^\circ$ ) synchrotron jet component.

losses dominate over the synchrotron losses (see Eq. 9 and Table 1). For runs 04, 14 and 15 the cutoff is smoother because the cooling rate above  $\gamma_c \sim 3 \cdot 10^3$  is affected by the Klein-Nishina regime, making it slower.

The spectrum above the cutoff is the standard cooling spectrum  $dN/d\gamma \propto \gamma^{-2}$ , and it changes to a steeper slope at higher energies. This is the result of the pair cascade developing in the jet. The cascade pairs affect the energy distribution making it steeper  $dN/d\gamma \propto \gamma^{-3}$  (e.g. Svensson 1987) above the break energy  $\gamma_b \sim 10^4 - 10^5$ . Pairs of lower energies produce photons that can freely escape from the jet and the cascade stops. We may note here that most of the pairs in the jet are produced by photons emitted in the jet. Such process does not contribute to the energy release. However, during the cascade the typical photon energy decreases, which leads to the increase of the probability of the photon escape to the external environment. This in turn increases the efficiency of the jet energy dissipation.

Fig. 10 shows the fraction of the jet energy content represented by generated pairs. The pair kinetic luminosity reaches 2–5 per cent of the initial jet power. The number ratio of generated electrons and positrons to that of the protons (in case of protons present jet) increases with the jet power and for runs 14–10 it is  $\tau_{\pm}/\tau_p = 0.017, 0.135, 0.63, 1.9, 4.0$ , respectively.

## 4 PROPERTIES AND LIMITATIONS OF THE MODEL

### 4.1 Non-linear effects

There are two kinds of non-linearity in the problem: one appears because of the feedback of radiation on the fluid, another is the result of the synchrotron emission which produces additional opacity for the high-energy photons. Here we consider the second one. The energy density of soft synchrotron radiation of pairs produced in the outer decelerated layers of the jet can exceed that of the external radiation described in §2.3.2. In Fig. 11 we compare the primary external radiation to the jet emission averaged over the volume. For run 31 the latter significantly exceeds the external radiation in both

components: longitudinal and isotropic. In this case the synchrotron emission of the jet becomes the main target for high-energy photons. For runs 01, 02, 10–12 and 35, the soft radiation associated with the jet is comparable with the original external radiation. In runs 03, 13–15 (also runs 41 and 42 for model B), despite  $\eta_j$  being the same, the jet emission at low energies is much smaller than the external radiation because the jet spectrum is harder. These cases can be treated as linear, so that the solution can be scaled to any lower jet power.

In the case of substantial non-linearity, the process becomes self-supporting. The external radiation becomes unnecessary, because the stronger synchrotron radiation plays the same role. Stawarz & Kirk (2007) have studied this kind of non-linearity using kinetic equations and found that a source of high-energy photons quenches itself at high compactness. In our case, we see that the efficiency decreases at high compactness and the final spectrum gets softer. We can expect that such tendency will continue with the increasing compactness.

The synchrotron emission from the jet scattered in the BLR (neglected in our simulations) can also affect the development of the cascade (Ghisellini & Madau 1996). The dominant contribution to the scattering is provided by the region of thickness  $\sim R_j$  immediately adjacent to the jet. If we associate the fraction of radiation scattered/reprocessed in BLR,  $\eta_s$ , with the optical depth through the region of size  $R$ , then the optical depth through the layer  $R_j$  for synchrotron photons moving at angle  $1/\Gamma_j$  is of the order  $\tau_{sc} \sim \eta_s \theta \Gamma_j$ . We can write now the scattered luminosity as

$$L_{s, \text{BLR}} = L_s \tau_{sc} = \eta_s (\eta_j L_d) \eta_s \theta \Gamma_j, \quad (29)$$

where  $\eta_s = L_s/L_j \lesssim 0.1$  is the fraction of the jet power emitted in the form of synchrotron radiation. Because the scattered synchrotron is escaping through the surface of  $\sim 4\pi\theta R^2$ , the ratio of its energy density to that of the BLR photons is then

$$\frac{U_{s, \text{BLR}}}{U_{\text{BLR}}} \approx \eta_s \eta_j \Gamma_j. \quad (30)$$

This shows that the scattered synchrotron can be important for large  $\eta_j$  or  $\Gamma_j$ .

#### 4.2 Temporal variability

In our simulations, we have assumed that the jet power and the Lorentz factor at the inlet does not change. However, because of the large non-linearity the output photon flux demonstrates large non-Poisson fluctuations at different time-scales. At the present level of numerical resolution, it is difficult to distinguish confidently between numerical fluctuations and natural chaotic behaviour of the non-linear dynamical system. We just would like to emphasise that the latter possibility is very probable.

The transversal gradient of the Lorentz factor,  $d\Gamma/dr$  affects the rate of the photon breeding in the same way as the slope of a sand pile affects sand avalanches. The emitted radiation feeds back on the jet dynamics, making the gradient smoother. Thus  $d\Gamma/dr$  balances near its critical value in the same way as the slope of the sand pile does when one pours sand on the top. It seems that we observe this in the cases of highest non-linearity when the soft radiation of the jet dominates the external soft radiation (runs 10 and 31, see Fig. 11). In these cases the radiation power is more sensitive to the transversal gradient of  $\Gamma$  because of a short free path of high-energy photons in this direction.

If we assume a large fluctuation in the jet power at a time-scale shorter than  $R/c\Gamma_j^2$ , the photon avalanche will be propagating along the jet and the observer will see a large increase in the luminosity partially because of the time compression. Simulations of strongly variable sources in the context of photon breeding model are left for future studies (see also SP06).

#### 4.3 Impact on the external environment

The high-energy photons produced in the jet interacting outside of the jet deposit their momentum into the external environment and therefore accelerate it. We neglect this acceleration assuming that the external matter is at rest. We can estimate at what density of the external matter this assumption is reasonable. Let the momentum deposited in a unit volume per unit time is  $\kappa(r, z) = dp/(dVdt)$ . Then, equating the work of the photon pressure force to the kinetic energy of the flow one gets the final velocity of the entrained medium (in non-relativistic limit):

$$\beta(r) = v/c = \left( \frac{2 \int \kappa(r, z) dR}{nm_p c^2} \right)^{1/2}, \quad (31)$$

where  $n \text{ cm}^{-3}$  is the particle density of the external medium. The required condition  $\beta \ll 1$ , allows to put the lower limit of the density of the environment:

$$n \gg n_{\text{cr}} \equiv \frac{2 \int \kappa(r, z) dR}{m_p c^2}. \quad (32)$$

During the simulations we accumulate the average deposited momentum  $\kappa$ . Its dependence on  $r$  is strong, and we present below the results for the layer closest to the jet,  $1 < r < 1.005$ . For run 31, we have  $\int \kappa(1 < r < 1.005, z) dR = 17 \text{ erg cm}^{-3}$ , which translates to  $n_{\text{cr}} = 2 \cdot 10^4 \text{ cm}^{-3}$ . The requirement (32) seems reasonable for the BLR, where the cloud density is about  $10^9 \text{ cm}^{-3}$  (Osterbrock & Ferland 2006) and even the mean density should not be much smaller. The critical densities for other runs are even smaller:  $n_{\text{cr}} = 10^3 \text{ cm}^{-3}$  for runs 02 and 12,  $n_{\text{cr}} = 30 \text{ cm}^{-3}$  for runs 04 and 14. For runs 41 and 42, the required density is  $n_{\text{cr}} = 10 \text{ cm}^{-3}$ , which is still reasonable at a parsec scale.

#### 4.4 Important phenomena beyond ballistic approximation

Our consideration is exact and model independent when concerning photons and pairs: their interactions, propagation, breeding, etc. at a given distribution of the fluid Lorentz factor and a given toroidal magnetic field. The only assumption we make is the spectrum and density of seed high-energy photons, this is however not important as their energy content is negligible and the system “forgets” their spectrum very soon.

On the other hand, our consideration is very approximate and is based on a simplified model when it concerns the fluid and the feedback of the particles on the fluid. How our simplifications affect the results and what we could obtain with a more realistic hydrodynamical treatment of the problem?

First, the pressure will redistribute the Lorentz factor of the fluid. This will hardly change significantly the process of particle breeding. More important, the formation of internal shocks at regions of maximal deceleration can increase the radiation efficiency by accelerating charged particles.

Then, we can expect that a turbulent layer near the jet boundary will be formed due to the large shear gradient of the Lorentz factor. The same can happen due to the Kelvin-Helmholtz instability of the boundary discontinuity (De Young et al. 1986), however for an ultra-relativistic jet this instability develops slowly. The radiative deceleration of the outer layer of the jet can generate the turbulent mixing layer much earlier. Then the turbulent layer should again contribute to the radiation due to diffusive particle acceleration (see Stawarz & Ostrowski 2003).

Finally, we ignore adiabatic heating of relativistic electrons while the jet (comoving) compression ratio in  $z$  direction is  $\sim \Gamma_j/\Gamma$ , where  $\Gamma$  is the Lorentz factor of the decelerated fluid. The account of the adiabatic heating is not simple, because the jet can expand in the transversal direction. The compression also leads to the amplification of the magnetic field  $B_j \propto 1/\Gamma$  (ignored in our simulations), which would in turn increase the role of synchrotron in the decelerated part of the jet.

The formation of shocks, turbulence and adiabatic heating of electrons, which can be caused by the jet deceleration, should increase the radiative efficiency of photon breeding mechanism, while the magnetic field amplification probably decreases it. These phenomena are interesting and should be studied in future simulations.

#### 4.5 Origin of the seed high-energy photons

In the presented simulations the energy content of the seed high-energy photons, which initiate the further evolution of the system, was taken to be 5–7 orders of magnitude smaller than the final steady-state total energy content in photons within the jet. Where these initial photons can originate from? They can be associated with the shock acceleration of charged particles in the jet. There is, however, a minimum possible source of high-energy, seed photons provided by the extragalactic gamma-ray background. The observed gamma-ray background intensity at Earth at  $\epsilon \gtrsim 10^5$  is  $\sim 10^{-6} \text{ GeV cm}^{-2} \text{ s}^{-1} \text{ str}^{-1}$  (Sreekumar et al. 1998), corresponding to the energy density  $6 \cdot 10^{-19} \text{ erg cm}^{-3}$ . This would give the energy  $\sim 3 \cdot 10^{31} R_{j,16}^3 \text{ erg}$  within the considered cylindrical volume of radius  $R_j$  and height  $20R_j$ .

We thus made a simulation (run 30) where the total energy of the seed high-energy photons in the simulation volume was 20 orders of magnitude smaller (approximately corresponding to the energy of the extragalactic gamma-ray background) than the jet en-

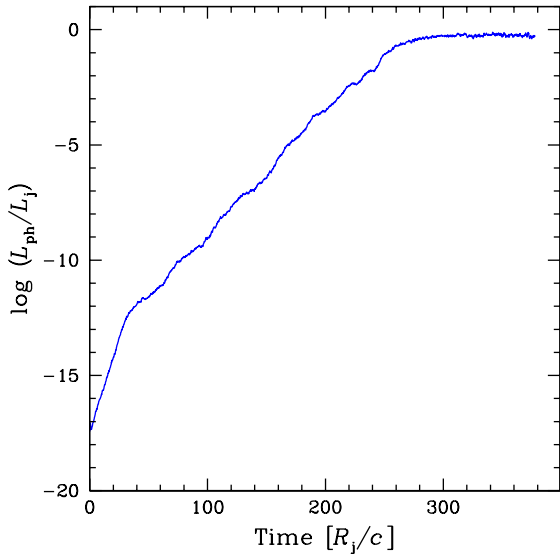


**Figure 12.** Fraction of the jet power converted into photons versus time for run 30. The initial density of the high-energy, seed photons corresponds to the extragalactic gamma-ray background.

ergy in the same volume  $E_j \sim 10^{51}$  erg. The result is shown in Fig. 12. The system passes 20 orders of magnitude in the total photon energy during  $300R_j/c \sim 3$  years. A jump at the very beginning of simulations corresponds to almost immediate conversion of seed photons into pairs (and their subsequent cooling) with the corresponding energy increase by a factor  $\Gamma_j^2 = 400$ . The photon energy grows exponentially with the time constant  $t_{pb} = 2.7$  at  $t \lesssim 25$  and  $t_{pb} = 8.2$  at later time. The rapid rise at  $t < 20$  corresponds to the growth of the photon avalanche as it moves downstream with the flow. At later times the growth is supported by the spatial feedback loop due to up-streaming photons. The final steady-state regime does not depend on the initial density of high-energy photons. This numerical experiment means that a jet, with parameters corresponding to run 30, would radiate half of its total energy in three years just due to the photon breeding starting off the extragalactic gamma-ray background.

## 5 ASTROPHYSICAL IMPLICATIONS

### 5.1 Spectral energy distribution of blazars

Blazars demonstrate two-component spectra. The low-energy component peaking in the infrared–X-ray range (the flares in the TeV blazars show hard X-ray spectra peaking above 100 keV) is traditionally interpreted as synchrotron radiation from relativistic electrons. The high-energy component is the Comptonized radiation from some seed soft photons. The spectra of low-luminosity objects (TeV blazars, BL Lacs) are well described by the synchrotron self-Compton (SSC) models. In high-luminosity blazars, both synchrotron and Compton components peak at lower energies (so called blazar sequence, Fossati et al. 1998; but see Giommi et al. 2007). The role of the external radiation (from BLR or dusty torus) in providing seed photons is probably more important, and the spectra can be described by external radiation Compton (ERC) model (Sikora et al. 1994, 1997). In all objects, the two components are rather well separated.

The spectra, predicted by the photon breeding model (see Fig.

6a), demonstrate similar features. At low luminosities and compactnesses (runs 04, 14–15), the mean Lorentz factor of the electron-positron distribution is large (see Fig. 9). In spite of the fact that (in the jet frame) the magnetic energy density is 1–2 orders of magnitude smaller than that of the isotropic radiation (i.e.  $\ell_B \ll \ell_{iso}\Gamma_j^2$ , see Table 1), the synchrotron power strongly dominates over the external Compton, because the external photons interact with the high-energy pairs in the Klein-Nishina regime. As most of the synchrotron photons are also above the Klein-Nishina cutoff  $\sim 1/\gamma$ , the SSC is weaker than the synchrotron.

At higher luminosities (and compactnesses), the high-energy photons produce a standard pair cascade. This reduces the mean energy per pair (see Fig. 9, runs 01–03, 10–13). At these compactnesses the pairs also cool more efficiently producing a cooling distribution  $dN/d\gamma \propto \gamma^{-2}$  (see Section 3.7), which changes to a steeper  $\gamma^{-3}$  behaviour at higher energies as a result of pair cascade. The latter part of the pair energy distribution is responsible for the flat part of photon spectrum (in  $E^2 dN/dE$  units).<sup>4</sup> The reduction of the mean pair energy results in a shift of the photon spectra to lower energies (Fig. 6a). It also leads to the increased role of the ERC, because now most of external photons interact with pairs in Thomson regime.

The properties of our model are the increasing role of the ERC over SSC and synchrotron with luminosity and a shift of the spectral peaks to lower energies. These are in general agreement with the observational trends. However, there are some discrepancies between the shapes of the theoretical and the observed spectral shapes. In our model at low luminosities, the synchrotron peak is in the 100 MeV – 1 GeV range, while it is normally observed to be in the X-ray range. One need to note here that the angle-dependent spectra at  $\theta \gtrsim 1/\Gamma_j$  have sharper features (see Fig. 7) and the synchrotron spectrum peaks at slightly lower energies than the spectrum averaged over  $10^\circ$  around the jet axis. Another possible reason for the discrepancy is that the electron distribution is broad and extends to very high energies. This is a consequence of our assumed spectrum of the soft isotropic radiation extending to a very low energy  $x_{min} = 10^{-9}$ . A narrower and harder distribution of external soft photons might make the injection function of pairs narrower and softer, so that the maximum pair energy is below  $\gamma_{max}$  given by equation (12), reducing thus the energy of the synchrotron cutoff.

At high luminosities, our model predict basically a single component where the synchrotron and ERC components are mixed, while there are clearly two separated components in the data. However, there is no consensus whether the two components are co-spatial. For example, the bright blazar 3C279 did not show almost any variability in the radio–optical band, when the gamma-ray flux changed by an order of magnitude (Wehrle et al. 1998). Thus the radio-to-optical emission in the high-luminosity sources can be produced in a separate region, far away from the black hole.

In our model, the pairs escaping from the region filled with soft photons still carry a considerable (a few per cent) fraction of the jet energy (see Fig. 10). If these pair are reheated at larger scales (e.g. by a diffusive acceleration by various plasma perturbations), where soft radiation field is weaker, they will radiate most of their energy in the form of synchrotron. At the expense of 3–5 per cent of the jet energy for pair reheating, the synchrotron peak observed

<sup>4</sup> One should note here that the pair cascade does not degrade the pair energies infinitely, when the energy of the photon in the jet frame drops below  $1/\Theta_{max}\Gamma_j \sim 10^4$ , it can easily escape and the cascade stops.

in low-peak blazars could be reproduced. If this hypothesis is valid then the high- and the low-energy peaks have different origin: the high-energy peak is a mixture of prompt synchrotron and Compton radiation of high-energy pairs in the fast cooling regime. The low-energy peak is the synchrotron radiation of pairs in a heating/cooling balance. In such a scenario the intensity of high- and low-energy peaks should correlate in time, but in a loose manner, the correlation should be stronger at longer time-scales.

## 5.2 Electron energy distribution in BL Lac objects and particle acceleration

One of the most often used in the recent years scenario for formation of the relativistic electrons, responsible for the observed emission, involves the diffusive (Fermi) acceleration at relativistic collisionless shocks (or shear layers). It has been claimed that the acceleration at relativistic shocks produces the power-law particle spectrum  $dN/d\gamma \propto \gamma^{-p}$  with a universal  $p = 2.2$  index (see e.g. Achterberg et al. 2001; Keshet & Waxman 2005) which is close to the value observed in BL Lacs (Ghisellini, Celotti & Costamante 2002). These results, however, were based on certain simplifying assumption regarding the scattering of particles by magnetic inhomogeneities. Using accurate Monte Carlo simulations with a more realistic magnetic field structure, Niemiec & Ostrowski (2006) demonstrated that no universal power-law is produced and questioned the role of the Fermi-type particle acceleration mechanism in relativistic shocks.

Using particle-in-cell simulations, Spitkovsky (2007) recently showed that the electrons can be heated by interaction with ion current filaments in the upstream region reaching almost an energy equipartition with protons. The low-energy cutoff appears at  $\gamma_{\min} \sim \frac{1}{5}\Gamma m_p/m_e$ . In internal shock model, the relative Lorentz factor of colliding shell is mildly relativistic and thus we expect  $\gamma_{\min} \sim 500$ . At this stage, it is too early to say whether the model would be able to produce a power-law electron distribution extending to very high energies.

The detailed fitting of the broad-band spectra of TeV blazars and low-power BL Lacs with the SSC model shows that the distribution of relativistic electrons injected to the system can be modelled as a power-law of index  $p \approx 2-2.5$  with the low-energy cutoff at  $\gamma_{\min} \sim 10^4-10^5$  and the high-energy cutoff at  $\gamma_{\max} \sim 10^6-10^7$  (Ghisellini et al. 2002; Krawczynski et al. 2002; Konopelko et al. 2003; Giebels et al. 2007).<sup>5</sup> Such a peaked distribution of injected electrons is not consistent with a diffusive process.

The photon breeding mechanism, on the other hand, predicts the injection spectrum to be bounded and to mirror (relative to  $m_e c^2$ ) the spectrum of the soft photon background, because the pairs in the jet are produced only by those high-energy photons that can interact with the soft photons. For example, if soft photons are from the accretion disc of maximum temperature  $\Theta_{\max}$ , the low-energy injection cutoff is at  $\gamma_{\min} \sim \Gamma_j/6\Theta_{\max}$  (see SP06; factor  $\Gamma_j$  comes from the Lorentz transformation to the jet frame). This cutoff should depend weakly on the luminosity and the black hole mass, which defines the characteristic emission radius, so that  $\Theta_{\max} \approx 10^{-5} L_{d,45}^{1/4} (M_{\text{BH}}/10^8 M_{\odot})^{-1/2}$  and thus we can predict that

$$\gamma_{\min} \sim 3 \cdot 10^5 \left( \frac{\Gamma_j}{20} \right) L_{d,45}^{-1/4} \left( \frac{M_{\text{BH}}}{10^8 M_{\odot}} \right)^{1/2}. \quad (33)$$

At high compactnesses, however, the synchrotron photons from the jet can provide enough opacity (see §4.1) and  $\gamma_{\min}$  may be smaller.

For the conditions appropriate for AGNs, the high-energy cutoff of the pair distribution  $\gamma_{\max}$ , that can participate in photon breeding, is defined by the different physics. An electron (or positron) of Lorentz factor higher than that given by equation (12) loses most of its energy to the synchrotron emission which escapes freely from the jet. Thus, at low compactnesses the pairs are injected to the jet between  $\gamma_{\min}$  and  $\gamma_{\max}$ . At high compactnesses, because of the higher opacity the Compton scattered photons cannot easily escape from the jet, producing a pair cascade which degrade their energy (see Fig. 9). The range of Lorentz factors of injected pairs as predicted by the photon breeding mechanism is in general agreement with observations of BL Lacs.

## 5.3 Jet power and composition

In many models of the high-energy emission from relativistic jets, the radiative efficiency is low because only internal energy of the jet can be dissipated (e.g. in internal shock model) and only a small fraction of the energy is transferred to the (high-energy) electrons. This leads to the large jet power requirements.

The photon breeding mechanism has important properties that significantly reduce the energy budget required: (i) it produces only electrons (positrons) of high Lorentz factors; (ii) it efficiently decelerates the jet, using thus most of its total power. Thus the radiative efficiency is extremely high, reaching in many cases 50–80 per cent.

The primary composition of the jet is not constrained if the photon breeding works, except the general requirement that it should not be dominated by cool pairs. Indeed, a dynamically important component of cold pairs can be excluded because of the absence of the bulk Compton scattering bump produced by such pairs in the soft X-rays (Sikora & Madejski 2000). Magnetically dominated jet is less favourable for photon breeding at  $\Gamma < 20$ , while for a larger Lorentz factor the radiative efficiency is not sensitive to the jet magnetisation. Independently of the primary jet composition the photon breeding loads the jet with a significant amount of relativistic pairs. The contribution of this pairs to the jet energy flux according to our simulation is 2–5 per cent (see Sect. 3.7). This is probably an underestimation as we do not take into account diffuse acceleration and adiabatic heating of pairs. The number ratio of generated electrons and positrons to protons (in the case of matter-dominated jet) may be related to the mean electron random Lorentz factor (as measured in the jet frame) and the radiative efficiency:

$$\frac{\tau_{\pm}}{\tau_p} \approx \frac{m_p \varepsilon_{\text{eff}}}{m_e \langle \gamma \rangle}. \quad (34)$$

For low-power jets, a typical  $\gamma \sim 10^5-10^6$ , and the number of generated pairs should be relatively small. At high powers, the mean pair energy decreases and the generated pairs dominate (Sect. 3.7). Thus, for high-power quasars the model predicts the number of pairs exceeding in number the protons, while dynamically the protons still dominate. This is consistent with the constraints on the pair content obtained from the X-ray spectra of blazars associated with quasars (Sikora & Madejski 2000).

<sup>5</sup> The high-luminosity objects require much lower energy electrons (Ghisellini et al. 2002), but this result may be biased because the electron distribution is obtained by the fitting of the synchrotron peak, which in reality may have nothing to do with the gamma-ray emitting zone.

#### 5.4 Gamma-ray emission sites

The arguments based on the gamma-ray transparency and the observed short time-scale variability constrain the gamma-ray emitting region in blazars to distances about  $\sim 10^{17}$  cm (Sikora et al. 1994). This distance is often associated with the BLR. In the internal shocks models, the shells of Lorentz factors  $\Gamma_1$  and  $\Gamma_2$  ejected from the central source and initially separated by the distance  $R_0$  collide at the distance  $R = R_0 \Gamma_1^2 / [1 - (\Gamma_1/\Gamma_2)^2]$ . Taking  $R_0 = 10^{15}$  cm ( $\approx 30R_S$  for a  $10^8 M_\odot$  black hole),  $\Gamma_1 = 10$  and  $\Gamma_2 \gg \Gamma_1$  we get  $R = 10^{17}$  cm. However, the agreement with the aforementioned constraints is rather coincidental, because the black hole mass can vary by 3–4 orders of magnitude and there is no physical theory yet predicting the assumed separation between the shells.

The photon breeding mechanism allows various emission sites. If the jet is already accelerated at distances  $\sim 100R_S$  from the black hole, the direct radiation from the accretion disc can serve as a target for high-energy photons for pair production and to trigger the photon avalanche. The photon-photon opacity through the jet is very large at these distances and the jet deceleration and radiative efficiency might be rather small, because only a very thin boundary layer is active. The escaping radiation should have a high-energy cutoff at tens of GeV rather than at TeV energies. At larger distances the disc radiation becomes more beamed along the jet and the disc photons do not interact anymore with the high-energy radiation produced in the jet. Thus the photon breeding stops. The jet now is, however, loaded with high-energy photons that can serve as seed high-energy radiation for the avalanche to be triggered at larger distances, where the conditions for photon breeding are satisfied. The natural scale for that is the position of the BLR, where the density of the isotropic soft photons is sufficiently high. As we showed in Section 3, the radiative efficiency here can be very large.

At even larger distances, the BLR photon density drops, the jet becomes transparent for high-energy photons and the photon breeding stops. If at the parsec scale, the jet is still relativistic enough, the process can start operating again on the infrared radiation from the dusty torus. The typical dust temperature (assuming a black body radiator) is  $\Theta_{\text{dust}} = kT_{\text{dust}}/m_e c^2 \approx 10^{-7} L_{\text{d},45}^{1/4} R_{\text{pc}}^{-1/2}$ . The pair-production optical depth is about

$$\begin{aligned} \tau_{\gamma\gamma} &= n_{\text{ph,dust}}(0.2\sigma_T)R_j = 30\eta_i(20\theta)\frac{L_{\text{d},45}}{R_{\text{pc}}\Theta_{\text{dust},-7}} \\ &= 30\eta_i(20\theta)L_{\text{d},45}^{3/4}R_{\text{pc}}^{-1/2}, \end{aligned} \quad (35)$$

where  $n_{\text{ph,dust}} = 0.37 U_{\text{dust}}/kT_{\text{dust}}$  is the number density of photons from the dust and  $\eta_i$  is the ratio of the dust to the disc luminosities. Thus, even for  $\eta_i$  of the order of a few percent, the photon breeding is effective at the parsec scale in bright quasars.

It has not escaped our attention that the jet may become active even further out: by interacting at kpc scale with the stellar radiation field and at  $\sim 100$  kpc with the cosmic microwave background radiation.

#### 5.5 The Doppler factor crisis in TeV blazars

The Doppler factors required by the homogeneous SSC models to describe the spectra of the blazars emitting at TeV energies (to avoid absorption by the infrared radiation), is rather large  $\delta \sim 20$ –50 (Ghisellini et al. 2002; Krawczynski et al. 2002; Konopelko et al. 2003; Giebels et al. 2007). Such high  $\delta$  values disagree with the small apparent velocities observed at the parsec scale in Mrk 421

and Mrk 501 (Marscher 1999; Piner & Edwards 2005) and other TeV blazars (Piner & Edwards 2004).

One proposed solution to this  $\delta$ -crisis (Tavecchio 2005) is that the jet Lorentz factor drops from 15 at the gamma-ray emitting, subparsec scale to  $\sim 4$  at the radio-emitting VLBI parsec scale (Georganopoulos & Kazanas 2003). Indeed, the apparent velocity is

$$\beta_{\text{app}} = \frac{\beta \sin \theta}{1 - \beta \cos \theta} \approx \frac{2\theta\Gamma^2}{1 + (\theta\Gamma)^2}, \quad (36)$$

where the last equality is valid for small  $\theta$ . For the viewing angle within the beaming pattern of the initial jet,  $\theta \lesssim 1/\Gamma_j$ , the apparent velocity of the decelerated jet with Lorentz factor  $\Gamma_f \ll \Gamma_j$  is

$$\beta_{f,\text{app}} \approx 2\theta\Gamma_f^2 \lesssim 2\frac{\Gamma_f^2}{\Gamma_j}. \quad (37)$$

Thus, deceleration of the jet to  $\Gamma_f < \sqrt{\Gamma_j/2}$  guaranties that the apparent motion is subluminal.

The question arises what is the mechanism that decelerates the jet at subparsec scale. A favoured by many mechanism for the transfer of bulk kinetic energy into particle kinetic energy and then to radiation involves internal shocks in the jet (Spada et al. 2001). However, it is known that the internal shocks are highly inefficient unless huge fluctuations of the Lorentz factors are involved (Beloborodov 2000), which seems unlikely. On the other hand, the photon breeding mechanism predict significant deceleration of the jet (see Table 1) and strong emission at subparsec scale, if the conditions for photon breeding are satisfied. The photon breeding thus may be responsible for jet deceleration and resolution of the  $\delta$ -crisis.

A different way to solve the  $\delta$ -crisis is to assume that the jet consists of a fast spine and a slow sheath (Chiaberge et al. 2000; Ghisellini et al. 2005). In this model a slower sheath having a softer spectrum dominates the emission in the radio band. The photon breeding mechanism, in a self-consistent way, produces exactly such a structure (Fig. 4) and the angular distribution (Fig. 8).

Thus, the jet behaviour predicted by the photon breeding mechanism unites the two proposals: it decelerates the jet at subparsec scales and produces a fast spine–slow sheath structure.

#### 5.6 Emission pattern

##### 5.6.1 Unification of BL Lacs and FR I radio galaxies

According to the unification scheme of radio-loud active galaxies (Urry & Padovani 1995), BL Lac objects are Fanaroff-Riley I (FR I) radio galaxies with their jets oriented close to the line of sight. The average Lorentz factor of the jets, derived by matching the luminosity functions and statistics of BL Lac and FR I (and B2) samples, was estimated to be  $\Gamma_j \sim 3$ –5 (Urry & Padovani 1995; Hardcastle et al. 2003). The core optical luminosities of BL Lacs are on average  $10^{4.5}$  times higher than those of FR I (Chiaberge et al. 2000) with the same extended radio luminosity. Associating the core emission with the jet, we again get rather low Lorentz factors  $\Gamma_j = 6$  or 4 for the continuous steady jet or a moving blob, respectively. These low  $\Gamma_j$  are in clear disagreement with much higher values of the Doppler factors required for BL Lacs to explain their gamma-ray emission.

Both decelerating (Georganopoulos & Kazanas 2003) and structured (Chiaberge et al. 2000; Ghisellini et al. 2005) jet models provide an explanation for the discrepancy. Because the photon breeding mechanism produces decelerating and structured jet,

it obviously is also capable of unifying BL Lacs with radio galaxies keeping high  $\Gamma_j$  to explain the gamma-ray emission. In blazars the emission from the fast,  $\Gamma_j \sim 20$ , spine dominates. In radio galaxies observed at large angles  $\theta \sim 1$  (see Fig. 8), the optical emission is produced in the slower sheath of  $\Gamma = 2-6$ .

### 5.6.2 Off-axis emission and the TeV emission from radio galaxies

As we have discussed above, the photon breeding mechanism naturally produces very broad beams of photons (see also Derishev et al. 2003; Derishev, Aharonian & Kocharovsky 2007). The gamma-ray emission at  $\theta \sim 1$  is produced in the external environment (see Fig. 8). The luminosity ratio between the nearly isotropic emission and the beamed emission at  $\theta \approx 1/\Gamma_j$  is about  $\Gamma_j^{-4}$  (two powers of  $\Gamma_j$  come from the energy amplification in the jet and two powers appear because of beaming). This ratio is  $\sim \Gamma_j^2/10$  larger than that predicted by equation (18). Thanks to the emission from the external medium, the nearby misaligned jets become observable in high-energy gamma-rays.

The central source of M87, which has the best studied jet, has a rather low disc luminosity of only  $\sim 10^{42} \text{ erg s}^{-1}$  (Biretta, Stern & Harris 1991). With the threshold  $L_d > 10^{43} R_{17} \text{ erg s}^{-1}$  for  $\Gamma = 20$  the photon breeding in model A is possible at  $R < 10^{16} \text{ cm}$ , which is only  $\sim 10 R_S$  for the estimated mass of the central black hole  $\sim 3 \cdot 10^9 M_\odot$  (Macchetto et al. 1997). At such a distance the photon breeding will operate on the direct disc radiation (model C). The implied distance is consistent with the detection of the rapid ( $\sim 10^5 \text{ s}$ ) variability of the TeV photon flux from M87 (Aharonian et al. 2006).

## 5.7 Observational appearance and volume dissipation

Most of the emission from the jet undergoing photon breeding comes from the regions of maximum gradient of  $\Gamma$ . In the steady-state, the volume emissivity contributing to the observed emission (at small angles to the jet) is

$$j(r, z) \propto \frac{d\Gamma(r, z)}{dz} \frac{\delta^3}{\Gamma}. \quad (38)$$

In the case of small luminosities (and small  $\Gamma_j$ ) only the outer layers of the jet suffer significant deceleration (see Fig. 4b, run 24), resulting in the limb-brightening, with most of the emission coming from large  $z$ , where the cascade had time to develop fully. The situation is more complicated at high luminosities (or large  $\Gamma_j$ ). The outer layers decelerate rapidly (see curves for runs 22, 23 in Fig. 5) making the emission limb-brightened at small  $z$ , while the layers close to the jet axis decelerate slower. Thus the emission from the core dominates at large  $z$ . At angles larger than  $\gtrsim 1/\Gamma_j$ , only slower, significantly decelerated layers contribute to the observed luminosity, and therefore we always would see the limb-brightened emission.

Our predictions are consistent with the observed limb-brightened morphology of the Mrk 501 jet at the parsec scale (Giroletti et al. 2004). Such a structure could result from the efficient deceleration and loading by relativistic pairs of the jet outer layers by the photon breeding at subparsec scale.

In spite of the fact, that deceleration is more efficient at the jet boundary, the energy dissipation can involve the whole volume of the jet. This is in a striking contrast to the Fermi-type diffusive acceleration, where only a narrow boundary layer is active.

## 6 CONCLUSIONS

The photon breeding mechanism can be an extremely efficient way of dissipating bulk energy of relativistic ( $\Gamma_j \gtrsim 10$ ) jet into high-energy radiation. In the case of a high luminosity AGNs and a powerful jet, the mechanism is very robust: it works at any value of the jet magnetic field and is not sensitive to the spectrum of external radiation. At high luminosities and Lorentz factors the mechanism should work almost inevitably, the only fact that can prevent the runaway photon breeding is a purely radial (along the jet) geometry of the magnetic field.

At the intermediate range of AGN luminosity,  $10^{43} < L_d R_{17} < 3 \cdot 10^{44} \text{ erg s}^{-1}$  and the Lorentz factor above 10, the mechanism still can work efficiently, but only at favourable conditions: a soft spectrum of external isotropic radiation and a weak (dynamically not important) magnetic field. When the Lorentz factor is below  $\sim 8$  or the AGN luminosity is below  $10^{43} R_{17} \text{ erg s}^{-1}$  the photon breeding mechanism does not work.

The mechanism can work in different astrophysical contexts: in the immediate vicinity of the accretion disc, in the broad line region (probably, most efficiently), and in the infrared radiation field produced by the dust at a parsec scale. There could be other sites for operation of the photon breeding mechanism (e.g. stellar radiation field at a kpc scale, cosmic microwave background radiation at a 100 kpc scale).

There exist a clear signature of the mechanism which can be observed by *GLAST* in the spectra of moderately bright blazars: a synchrotron cutoff at a few GeV range.

There exist some problem with the straightforward interpretation of the blazar spectra. The low-energy synchrotron peak reproduced by our simulations is less prominent than the one observed in the spectra of gamma-ray quasars. An additional mechanism of gradual pair reheating is necessary. This could be associated with a diffusive Fermi acceleration of pairs produced by the photon breeding by fluid perturbations. Such reheating mechanism should have a moderate energy budget and seems very natural after a strong impact of radiation on the jet. Importantly, the photon breeding solves the problem of injection of relativistic electrons for Fermi acceleration: they are already produced by high-energy photons.

Fast deceleration of the jet resulting in a large radial gradient of the Lorentz factor can form a structure with the fast spine and slower sheath which is implied by various observations. Particularly, the deceleration and the jet structuring can solve the contradiction between a requirement of the large Doppler factor in the gamma-ray emitting region and the low Lorentz factor of jets in BL Lacs derived from the radio and optical observations.

Despite the fact that the photon breeding mechanism has not been known before and may seem somewhat exotic, it is actually much simpler in the description than the diffusive Fermi acceleration, which depends on complicated plasma phenomena. Once the velocity pattern for the fluid, the magnetic field and the external radiation field are specified, the fate of each high-energy photon and its descendants can be reproduced (in statistical sense) from first principles, because the interaction cross-section are known with high accuracy. The question whether a photon produces a runaway avalanche or not, can be answered exactly. However, there still remain some details which require a more elaborated treatment of the fluid dynamics and a more complete model for the jet. Particularly, it would be important to study the jet launch, the photon breeding, and the jet deceleration with the resulting gamma-ray emission in one numerical experiment.

**ACKNOWLEDGMENTS**

The work is supported by the Russian Foundation for Basic Research grant 07-02-00629-a, the Magnus Ehrnrooth Foundation, the Vilho, Yrjö and Kalle Väisälä Foundation, and the Academy of Finland grants 109122, 110792 and 112982. We thank Anatoly Spitkovsky for comments.

**REFERENCES**

- Aharonian F. et al., 2006, *Sci*, 314, 1424  
 Achterberg A., Galant Y. A., Kirk J. G., Guthmann A. W., 2001, *MNRAS*, 328, 393  
 Arav N., Begelman M.C., 1992, *ApJ*, 401, 125  
 Beloborodov A. M., 2000, *ApJ*, 539, L25  
 Biretta A., Stern C. P., Harris D. E., 1991, *AJ*, 101, 1632  
 Chiaberge M., Celotti A., Capetti A., Ghisellini G., 2000, *A&A*, 358, 104  
 Derishev E. V., Aharonian F. A., Kocharovskiy V. V., Kocharovskiy V. V., 2003, *Phys Rev D*, 68, 043003  
 Derishev E. V., Aharonian F. A., Kocharovskiy V. V., 2007, *ApJ*, 655, 980  
 Dermer C. D., 1995, *ApJ*, 446, L63  
 Dermer C. D., Schlickeiser R., 1993, *ApJ*, 416, 458  
 De Young D. S. et al., 1986, *ApJ*, 307, 62  
 Fossati G., Maraschi L., Celotti A., Comastri A., Ghisellini G., 1998, *MNRAS*, 299, 433  
 Georganopoulos M., Kazanas D., 2003, 594, L27  
 Ghisellini G., Madau P., 1996, *MNRAS*, 280, 67  
 Ghisellini G., Celotti A., Costamante L., 2002, *A&A*, 386, 833  
 Ghisellini G., Tavecchio F., Chiaberge M., 2005, *A&A*, 432, 401  
 Giebels B., Dubus G., Khélifi B., 2007, *A&A*, 462, 29  
 Giommi P. et al., 2007, *A&A*, 468, 97  
 Giroletti M. et al., 2004, *ApJ*, 600, 127  
 Hardcastle M. J., Worrall D. M., Birkinshaw M., Canosa C. M., 2003, *MNRAS*, 338, 176  
 Jorstad S. G., Marscher A. P., Mattox J. R., Wehrle A. E., Bloom S. D., Yurchenko A. V., 2001, *ApJS*, 134, 181  
 Kaspi S., Maoz D., Netzer H., Peterson B. M., Vestergaard M., Jannuzi B. T., 2005, *ApJ*, 629, 61  
 Keshet U., Waxman A., 2005, *Phys. Rev. Lett.*, 94, 111102  
 Krawczynski H., Coppi P. S., Aharonian F., 2002, *MNRAS*, 336, 721  
 Konopelko A., Mastichiadis A., Kirk J., de Jager O. C., Stecker F. W., 2003, *ApJ*, 597, 851  
 Lind K. R., Blandford R., 1985, *ApJ*, 295, 358  
 Lyutikov M., 2003, *NewAR*, 47, 513  
 Macchetto F., Marconi A., Axon D. J., Capetti A., Sparks W., Crane P., 1997, *ApJ*, 489, 57  
 Marscher A. P., 1999, *Astrophys. J.*, 11, 19  
 Mukherjee R., et al., 1997, *ApJ*, 490, 116  
 Niemiec J., Ostrowski M., 2006, *ApJ*, 641, 984  
 Peterson B. M. 1993, *PASP*, 105, 247  
 Piner B. G., Edwards P. G., 2004, *ApJ*, 600, 115  
 Piner B. G., Edwards P. G., 2005, *ApJ*, 622, 168  
 Rawlings S., Saunders R., 1991, *Nat*, 349, 138  
 Rees M., 1978, *MNRAS*, 184, L61  
 Rybicki G. B., Lightman A. P., 1979, *Radiative Processes in Astrophysics*. Wiley, New York  
 Osterbrock D. E., Ferland G. J., 2006, *Astrophysics of gaseous nebulae and active galactic nuclei*. University Science Books, Sausalito, CA  
 Sikora M., Begelman M. C., Rees M. J., 1994, *ApJ*, 421, 153  
 Sikora M., Madejski G., 2000, *ApJ*, 534, 109  
 Sikora M., Madejski G., Moderski R., Poutanen J., 1997, *ApJ*, 484, 108  
 Spada M., Ghisellini G., Lazzati D., Celotti A., 2001, *MNRAS*, 325, 1559  
 Spitkovsky A., 2007, *ApJ*, submitted (astro-ph/ arXiv: 0706.3126v1)  
 Stawarz L., Kirk J. G., 2007, *ApJ*, 661, L17  
 Stawarz L., Ostrowski M., 2003, *NewAR*, 47, 521  
 Stern B. E., 1985, *Astron. Zh.*, 62, 529  
 Stern B. E., 2003, *MNRAS*, 345, 590  
 Stern B. E., Poutanen J., 2006, *MNRAS*, 372, 1217  
 Stern B. E., Begelman M. C., Sikora M., Svensson R., 1995, *MNRAS*, 272, 291  
 Sreekumar P. et al., 1998, *ApJ*, 493, 547  
 Svensson R., 1987, *MNRAS*, 227, 403  
 Tavecchio F. 2005, in Novello M., Perez Bergliaffa S., Ruffini R., eds, *The Tenth Marcel Grossmann Meeting*. World Scientific Publishing, Singapore, p. 512  
 Urry C. M., Padovani P., 1995, *PASP*, 107, 803  
 Wehrle A. C. et al., 1998, *ApJ*, 497, 178